Opto-Electronic Advances

CN 51–1781/TN ISSN 2096–4579 (Print) ISSN 2097–3993 (Online)

Ferroelectric domain engineering of lithium niobate

Jackson J. Chakkoria, Aditya Dubey, Arnan Mitchell and Andreas Boes

Citation: Chakkoria JJ, Dubey A, Mitchell A, et al. Ferroelectric domain engineering of lithium niobate. *Opto-Electron Adv* **8**, 240139(2025).

https://doi.org/10.29026/oea.2025.240139

Received: 7 June 2024; Accepted: 3 September 2024; Published online: 2 January 2025

Related articles

Spatio-temporal isolator in lithium niobate on insulator

Haijin Huang, Armandas Balčytis, Aditya Dubey, Andreas Boes, Thach G. Nguyen, Guanghui Ren, Mengxi Tan, Arnan Mitchell

Opto-Electronic Science 2023 **2**, 220022 doi: 10.29026/oes.2023.220022

Soliton microcomb generation by cavity polygon modes

Botao Fu, Renhong Gao, Ni Yao, Haisu Zhang, Chuntao Li, Jintian Lin, Min Wang, Lingling Qiao, Ya Cheng

Opto-Electronic Advances 2024 **7**, 240061 doi: 10.29026/oea.2024.240061

More related article in Opto-Electronic Journals Group website

OEA Opto-Electronic Advances

http://www.oejournal.org/oea

OE_Journal

@OptoElectronAdv

Opto-Electronic Advances

Review

January 2025, Vol. 8, No. 1

DOI: 10.29026/oea.2025.240139 CSTR: 32247.14.oea.2025.240139

Ferroelectric domain engineering of lithium niobate

Jackson J. Chakkoria[1,2†*], Aditya Dubey[1,2†], Arnan Mitchell[1,2] and Andreas Boes[2,3,4]

Lithium niobate (LN) has remained at the forefront of academic research and industrial applications due to its rich material properties, which include second-order nonlinear optic, electro-optic, and piezoelectric properties. A further aspect of LN's versatility stems from the ability to engineer ferroelectric domains with micro and even nano-scale precision in LN, which provides an additional degree of freedom to design acoustic and optical devices with improved performance and is only possible in a handful of other materials. In this review paper, we provide an overview of the domain engineering techniques developed for LN, their principles, and the typical domain size and pattern uniformity they provide, which is important for devices that require high-resolution domain patterns with good reproducibility. It also highlights each technique's benefits, limitations, and adaptability for an application, along with possible improvements and future advancement prospects. Further, the review provides a brief overview of domain visualization methods, which is crucial to gain insights into domain quality/shape and explores the adaptability of the proposed domain engineering methodologies for the emerging thin-film lithium niobate on an insulator platform, which creates opportunities for developing the next generation of compact and scalable photonic integrated circuits and high frequency acoustic devices.

Keywords: lithium niobate; ferroelectric; domain engineering; lithium niobate on insulator; domain visualization; periodic poling; quasi-phase matching; acoustic

Chakkoria JJ, Dubey A, Mitchell A et al. Ferroelectric domain engineering of lithium niobate. *Opto-Electron Adv* **8**, 240139 (2025).

Introduction

Lithium Niobate (LN) is a synthetically grown crystal, with its origins traced back to 1928 when it was first synthesised and characterised by Zhachariasen[1]. Later, in 1965, Ballman[2] achieved a breakthrough by successfully cultivating large, single crystals with excellent homogeneity while employing the Czochralski technique for growth. Nassau[3] and other researchers further propelled the exploration of LN's material properties in 1966. Since its early development, LN has evolved into a remarkably compelling and well-established material, finding widespread utility across an extensive range of optical and acoustic applications. This wide usage of LN in numerous applications can be explained by its rich array of material characteristics, exhibiting strong pyroelectric, piezoelectric, electro-optic, photorefractive, acousto-optic, photovoltaic, and nonlinear optical properties[4–10]. Furthermore, LN has a wide optical transparency window (350 nm to 5 μm)[11,12] , providing the means to utilise the attractive material properties over a wide spectrum,

[1]Integrated Photonics and Applications Centre, School of Engineering, RMIT University, Melbourne, VIC 3001, Australia; [2]ARC Centre of Excellence in Optical Microcombs for Breakthrough Science (COMBS); [3]School of Electrical and Mechanical Engineering, The University of Adelaide, Adelaide, SA 5005, Australia; [4]Institute for Photonics and Advanced Sensing, The University of Adelaide, Adelaide, SA 5005, Australia.
[†]These authors contributed equally to this work.
*Correspondence: JJ Chakkoria, E-mail: s3881290@student.rmit.edu.au

Received: 7 June 2024; Accepted: 3 September 2024; Published online: 3 January 2025

Open Access This article is licensed under a Creative Commons Attribution 4.0 International License.
To view a copy of this license, visit http://creativecommons.org/licenses/by/4.0/.

© The Author(s) 2025. Published by Institute of Optics and Electronics, Chinese Academy of Sciences.

which has enabled record-breaking experimental demonstrations in fundamental science[12]. LN's maturity has also enabled many commercial LN devices, such as acoustic frequency bandpass filters for mobile communications[13] and high-speed electro-optical modulators that helped to underpin the Internet[14].

A material property that distinguishes it from many other acoustic and optical materials is that it is possible to invert the spontaneous polarization of the crystal with mature methods that offer excellent spatial resolution, while the inverted ferroelectric domains are stable over the long term. The local inversion of the crystal's spontaneous polarization is also referred to as ferroelectric domain engineering or simply 'domain engineering'. LN crystals that have a periodic domain pattern are also often referred to as periodically poled LN (PPLN). Being able to domain engineer LN is very attractive as it provides an additional degree of freedom for designing acoustic and optical devices. For example, periodically poled LN can be used in acoustic devices to generate monolithically uniform phononic crystals[15] or for the generation of acoustic waves with simple coplanar electrodes[16]. In optical applications, periodically poled LN is often used to quasi-phase match different wavelengths and/or modes to enable efficient nonlinear optical interaction, for example, for second harmonic generation[17].

In the last few years, LN has attracted renewed interest, particularly from the integrated photonic community, due to the commercial availability of thin-film LN on insulator (LNOI). This integrated photonic platform has sparked a renaissance in exploiting the optical material properties of LN as it enables low-loss optical waveguides with much stronger confined optical modes compared to the traditional diffusion-based waveguides in bulk LN[12,18,19], enabling more compact and complex integrated optical devices with more than an order of magnitude improved nonlinear optical efficiencies[20–22] and more efficient and faster electro-optical modulators[23–25]. In LNOI, ferroelectric domain engineering also plays a crucial role in designing optical circuit components.

This renewed interest in lithium niobate sparked by LNOI is the primary motivation for this review, providing a comprehensive summary of the many different ferroelectric domain engineering methods that have been developed for LN over the past decades and to assess their suitability for the LNOI platform. The review paper is structured as follows: Section *Lithium niobate crystal properties* highlights the material properties of lithium niobate (LN) crystals. Section *Visualization of domain pattern* provides an overview of the different methodologies for visualizing ferroelectric domain patterns in LN. Section *Domain engineering methods* outlines diverse domain engineering techniques. Section *Applications of domain engineered LN* comprehensively addresses the applications of domain-engineered LN. An outlook and summary with future perspectives are presented in Sections *Outlook* and *Summary*.

Lithium niobate crystal properties

LN's many attractive material properties and the ability to ferroelectrically domain engineer LN are closely linked to its crystal structure[26]. An overview of LN's crystal structure, how LN's crystal structure changes when the spontaneous polarization is inverted, and the influence of doping and defects is provided in this section. A detailed description of LN crystal properties can be found in ref.[27,28].

Crystal structure

LN's crystal structure was first described in the mid-1960s by Abraham et al. at Bell laboratories with data obtained from various characterization methods such as X-ray diffraction[29] and neutron scattering[30]. They found that LN exhibits a Trigonal (Rhombohedral) crystal system below the Curie temperature (T_c ~1145 °C) and that it belongs to the R3c space group with threefold symmetry about the polar axis (c-axis or optical axis)[31]. LN is also known as oxygen octahedral ferroelectric since six octahedral are stacked, which share close-packed planes to form a unit cell and exhibit ferroelectric properties[32,33]. Above the Curie temperature, LN belongs to the −3 m point group and behaves as a paraelectric material.

The phase transition in LN is caused by the slight displacement of the Nb cation from the center of the octahedron to an asymmetric position (displacement is 0.258 Å at room temperature, 1 Å=10^{-10} m) and displacement of Li (0.690 Å) from the octahedron, as illustrated in Fig. 1(c). The displacement of cations gives rise to a permanent dipole moment (spontaneous polarization) within the crystal and ferroelectric properties below the Curie temperature. The cations of LN crystal are arranged in a particular order in the octahedron as Li, Nb, Vacancy, Li, Nb, Vacancy, …. along the *Z*-axis, as can be seen in Fig 1(c). The non-centrosymmetric crystal structure, which causes the permanent dipole moment, gives rise to LN's interesting $\chi^{(2)}$ material properties as well as its negative uniaxial birefringence (n_e<n_o).

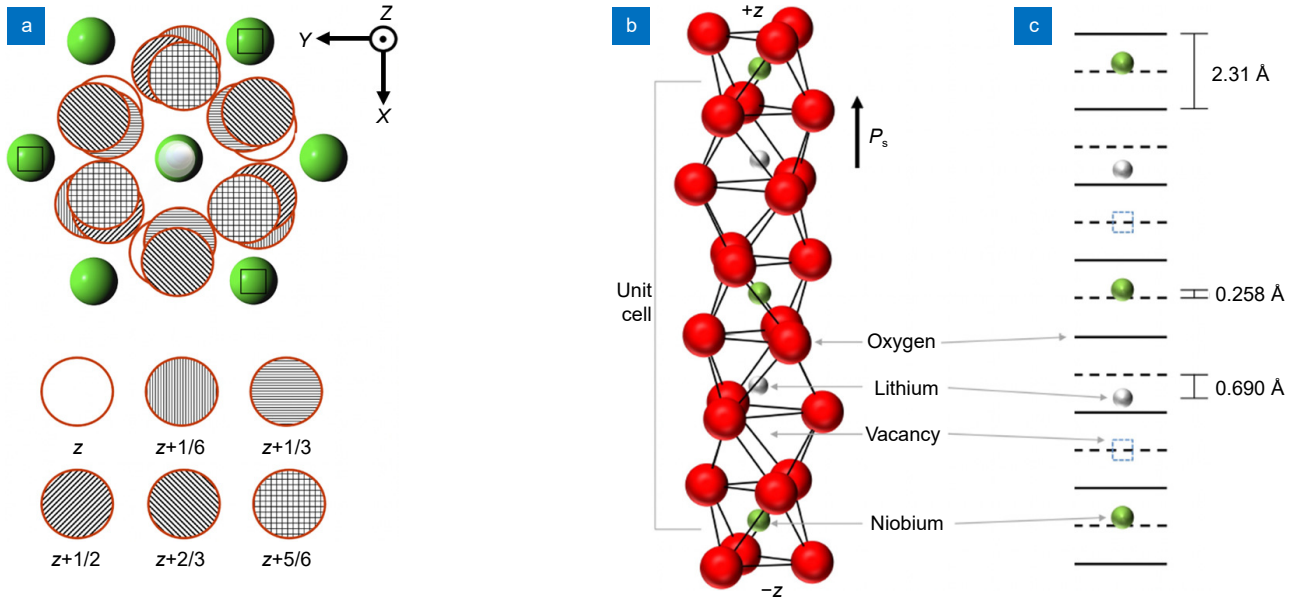

Fig. 1 | (**a**) Top view of the relative arrangement of oxygen atoms about the Li and Nb atoms in LN, corresponding to the sequence of the unit cell. (**b**) Side view illustration of the LN unit cell crystal structure. (**c**) The relative position of the cations (Li and Nb) in the crystal structure in relation to the oxygen plane is represented by black lines. The dashed lines indicate the center position between two oxygen planes. Figures redrawn from: (a) ref.[34], CRC Press ; (b, c) ref.[35], Elsevier.

Domain inversion

The ferroelectric crystal properties of LN[36] permit the inversion of its spontaneous polarization (P_s) in a process known as domain inversion. The different methods that can be used for achieving domain inversion in LN are described in Section *Domain engineering methods*. The commonality of the different domain inversion methods is that an electric field is either being applied to the crystal by using external sources or being generated within the crystal, where the electric field is aligned along the polar axis (*c* or *Z*) of the LN crystal in the opposite direction and with a field strength higher than the coercive field of LN. The coercive field[33] can be described as the electric field strength required to invert the polarization of a ferroelectric material. In LN, the inversion of the ferroelectric domain results in an inversion of the dipole moment i.e., the spontaneous polarization (P_s)[28] with a 180° phase shift and formation of a domain wall to separate two areas with opposing dipole moments. Only two polarization states can exist in LN[28]. The direction of spontaneous polarization changes when the niobium cation in the octahedron is displaced to a new asymmetric position, and the lithium cation undergoes a more significant transition and moves to the next, vacant octahedron through the closed-packed oxygen plane[28]. An illustration of the crystal structure before and after domain inversion is given in Fig. 2. In LN, domains typically grow in hexagonal cross-sections in the *X*-*Y* plane, with the domain walls having a preferential axis that tends to orient along the *Y*-axis. Such anisotropic domain propagation of domain walls can be utilized by patterning the electrode parallel to the *Y*-axis for better control over the domain pattern[28,37].

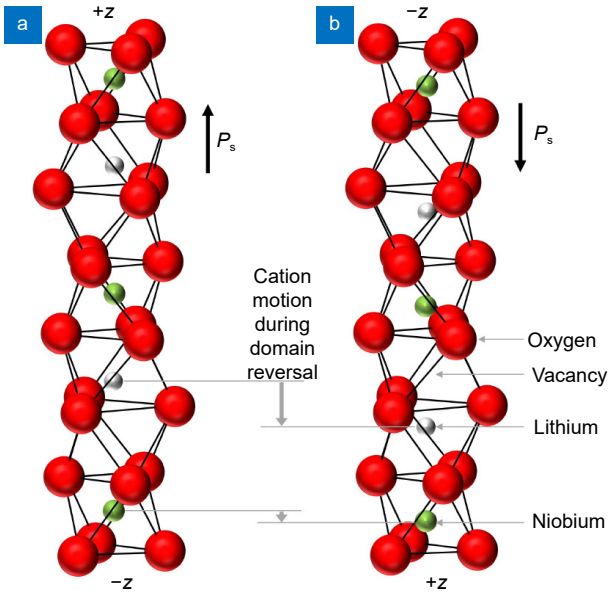

Fig. 2 | (**a**, **b**) Movement of the Li and Nb ions during domain inversion. The Nb ions undergo a small displacement within their oxygen octahedrons, whereas the Li ions undergo a larger displacement through the close-packed oxygen planes into the adjacent, vacant oxygen octahedrons. Figure redrawn from ref.[33], Annual Reviews.

Defects and doping

The LN composition can have a significant influence on the domain inversion process. The most widely used LN composition is congruent LN or CLN (i.e., ~Li-48.45% and ~Nb-51.55%)[28], which is grown out of a melt by the Czochralski method[2], and allows the growth of LN wafers with diameters of up to 150 mm. Advancements in the crystal growth technique by using Double Crucible Czochralski growth (DCCZ) paved the way for the realization of near stoichiometric LN or NSLN (i.e., ~Li-50% and ~Nb-50%)[32]. The composition difference in CLN and near NSLN has a strong influence on the various material properties, but arguably the most important one for domain engineering is the coercive field E_c, which is around 21 kV/mm in CLN, while in NSLN it is 4 kV/mm[33]. This means the electric field required to cause domain inversion is about a factor of 5 lower in NSLN compared to CLN. It should also be noted that CLN can be doped with materials such as MgO and ZnO[28,38], which can occupy the vacancies caused by defects, resulting in similar material properties to NSLN, such as the reduction in the coercive field strength when compared to CLN. This highlights that it is important to consider the LN composition in the domain engineering process.

Visualization of domain pattern

In this section, we introduce methods used for visualizing ferroelectric domain patterns in LN crystals. Visualizing the domain pattern is required to assess the inverted domains' quality, for example, when the domain engineering process (Section *Domain engineering methods*) is being optimized. Each domain visualization method has its advantages and disadvantages, and considerations for choosing the most suitable method include the imaging speed, resolution, in-situ or ex-situ and whether the method is invasive or non-invasive to the LN crystal. The domain visualization methods introduced in this section are selective chemical etching, piezoresponse force microscopy (PFM), second harmonic generation (SHG) microscopy, electro-optic imaging microscopy and polarization microscopy. It is important to note that this is not an exhaustive list of domain visualization methods but represents some of the most commonly used ones for LN crystals.

Selective chemical etching

Selective chemical etching of LN crystal faces is a method that translates the ferroelectric domain pattern into a topography, which then is imaged by methods such as optical microscopy and scanning electron microscopy (SEM). An example of the process flow for visualizing domain patterns can be seen in Fig. 3, where the distinctive etch rates of the $+Z$ and $-Z$ faces of LN reveal the domain pattern of a periodically poled LN sample. Different etchants have been investigated for their differential crystal facet etching rates, including mixtures of hydrogen peroxide (H_2O_2) and sodium hydroxide (NaOH)[39], hydrofluoric acid[28] (HF) with potassium hydroxide (KOH)[28,39], HF acid with potassium permanganate ($KMnO_4$)[28,39], HF acid with nitric (HNO_3)[40] and 'pure' 48% HF. For Z-cut LN, their study revealed that in each case, the $+Z$ face remained unetched, while the $-Z$ face was etched (e.g., the etch rate of the $-Z$ face is ~0.8 μm/h in 48% HF at a room temperature). Selective chemical etching can also be used for translating the domain pattern of Y-cut LN crystals into a topography, as the Y faces of LN possess different etching rates. Here, the $-Y$ face etches faster (~0.08–0.11 μm/h) than the $+Y$ face (~0.04–0.05 μm/h) when etched in pure HF at room temperature[41,42]. LN's X faces do not show signs of differential etching; as such, chemical etching is unsuitable for translating domain patterns into a topography in X-cut LN samples. The differential etching of the LN crystal facets is speculated to be caused by surface protonation with an observation that fluorine ions (negatively charged) diffuse preferentially into the $+Z$ face of LN crystals compared to the $-Z$ face, where the etching is

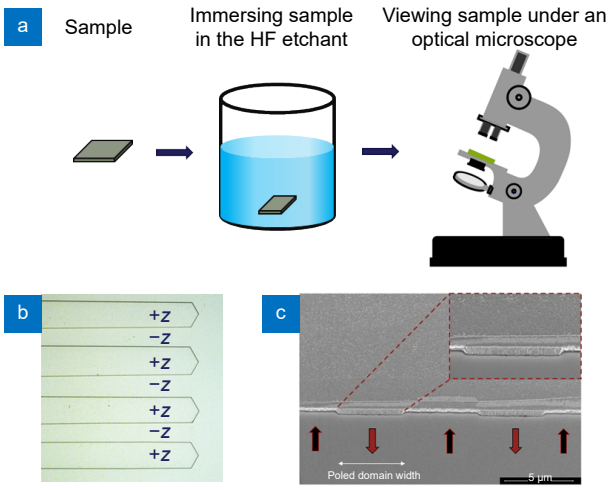

Fig. 3 | (**a**) Illustration of the domain visualization process using selective chemical etching. (**b**) Periodically poled bulk LN (Z-cut) viewed under an optical microscope. (**c**) Image of etched LNOI (X-cut) sample observed with an SEM.

faster due to easier absorption of positively charged proton[28,43].

It is worth noting that this domain visualization method does not require expensive, sophisticated imaging equipment, and domain features can readily be imaged by standard optical microscopy. If the domain features are below the resolution of optical microscopes, higher-resolution imaging technologies such as SEM can be used. Selective chemical etching combined with microscopy is particularly suitable for imaging large area domain patterns and for assessing the uniformity of such large area domain patterns, as imaging with optical microscopy or SEM is relatively quick. However, it is important to note that selective chemical etching is an invasive process that alters the surface of LN and can, therefore, be destructive if the sample's surface quality is important.

Selective chemical etching is also suitable for the visualization of domain patterns in thin film LNOI. In *Z*-cut and *Y*-cut thin films, the domains can be imaged from the top right after the differential HF etching, which is not possible in *X*-cut thin films. However, the domain profiles in *X*-cut LNOI can also be imaged by forming a cross-section via dry etching, which exposes the crystallographic *Z*-face, followed by a selective chemical etching process[37]. An example of such a cross-section can be seen in Fig. 3(c). This method also provides insights into depth of the inverted domains, which is an important parameter impacting the efficiency of nonlinear frequency conversion in periodically poled waveguides. It should be noted that the buffer SiO_2 layer experiences a higher etch rate compared to the -*Z*-face of the LN crystal, which can cause under-etching of the LN thin-film.

Piezoresponse force microscopy

Piezoresponse force microscopy (PFM) was first demonstrated by Guenther et al. in 1992[44], allowing the non-invasive imaging of ferroelectric domain patterns. PFM uses a standard scanning probe microscope operated in contact mode with a conductive cantilever/tip. In this method, a voltage is applied to the conductive cantilever (see Fig. 4(a)), causing a periodic deformation in the localized area on the LN surface due to the inverse piezoelectric effect[45,46]. This periodic deformation or vibration is picked up by the cantilever. When the cantilever is scanned from one ferroelectric domain (e.g., +*Z* face) to another (e.g., −*Z* face), the cantilever will experience a change in the phase of the vibration signal (180° phase shift), while the amplitude of the vibration signal remains the same (see Fig. 4(b)). Thus, one can use the phase information generated by the PFM technique to identify a change in crystal polarization. This information can be used to create an image of the domain pattern when a raster scan is performed across the area of interest (see Fig. 4(c)). The small tip of the PFM enables measurements of domain features with sub-micrometers and even a few nanometer dimensions with high precision[47–49].

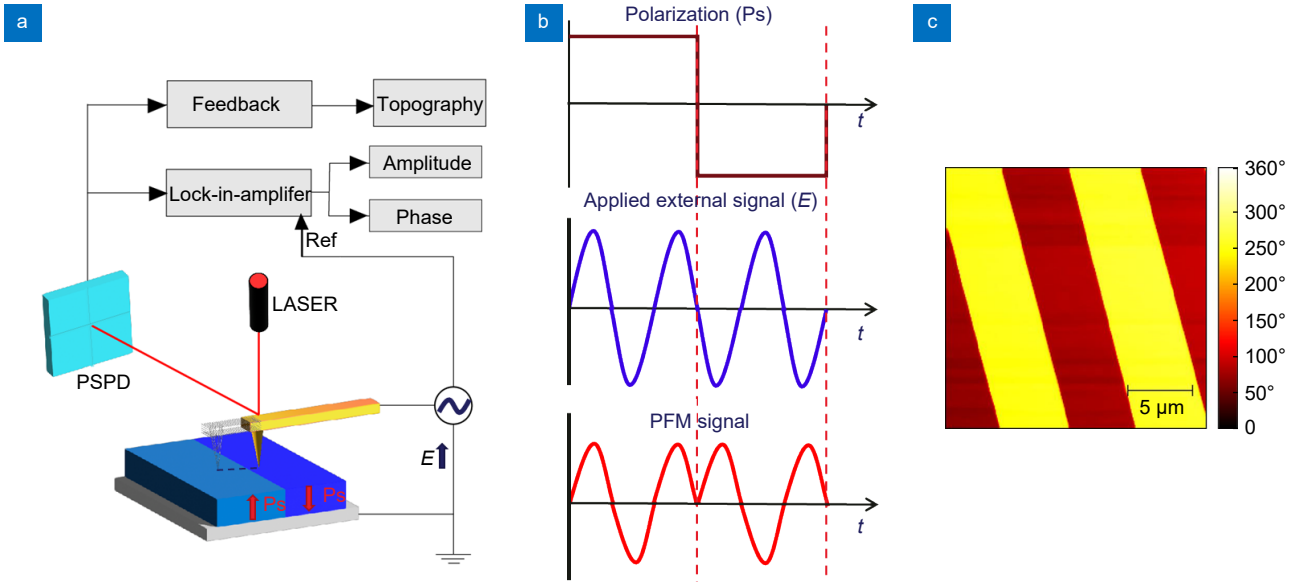

Fig. 4 | (**a**) Schematic for contact-mode scanning probe microscopy used for PFM. (**b**) Illustration of the PFM signal, resulting from the orientation of the spontaneous polarization and the applied external voltage to the conductive cantilever. (**c**) PFM image of a periodically poled LN crystal.

One of the drawbacks of this domain visualization technique is that it can be time-consuming to image domain patterns of a large sample due to the limited scanning speed of the tip. One should also give importance to the selection of the conductive tip and the amount of applied voltage. PFM can also be used for imaging domain patterns on all crystal faces of bulk LN and LNOI samples[47–50]. More information about this domain visualization technique can be found in the review article by E. Soergel[45,46].

Second harmonic generation microscopy

Second harmonic generation (SHG) microscopy is a non-destructive in-situ 3-D visualization method to image ferroelectric domain patterns or domain walls with high resolution by using scanning optical microscopy. Here, femtosecond light pulses, typically in the near-infrared wavelength range, are tightly focused into the LN crystal. The high intensity of the tightly focused light pulses in the LN crystal results in the generation of a second harmonic (SH) signal, which is either collected in the backward or in a forward direction. Raster scanning the focal spot and recording the SH signal is used to generate an image[51,52]. In transparent samples, detection in both directions is possible, whereas in thin film LNOI samples with substrates such as silicon, the SH signal can only be detected in the backward direction due to the non-transparent properties of silicon for the SH wavelength[53]. One can distinguish between three commonly used operation modes of SHG microscopy, namely (i) interference SHG microscopy, (ii) non-interference SHG microscopy, and (iii) Cherenkov SHG microscopy. In the following, a brief overview of the methods is given.

In the interference SHG microscopy[53–55], light from a high peak-power laser (e.g., femtosecond laser) is focused into the LN crystal by using a high numerical aperture objective. The high peak power of the pulse generates a non-phase matched nonlinear optical second harmonic signal in the LN crystal, which propagates collinearly with the fundamental beam (see Fig. 5(b)). The phase of the SH signal generated in the LN depends on the crystal polarization, which means that two opposing polarized areas produce SH signals with a π phase shift. As the phase of the SH signal cannot be directly measured, interference SHG microscopy uses SH light generated in a reference nonlinear optic crystal to interfere with the SH signal from the sample under investigation. The constructive and destructive interference of the SH signals turns the phase information into amplitude information, causing opposing polarized areas in LN crystals to appear bright or dark (see Fig. 5(c)), which can be used for imaging ferroelectric domain patterns in LN crystals.

In non-interference SHG microscopy, no reference SH light is used for imaging. Instead, the collinear SH signal vanishes when a focused laser pulse is scanned across a

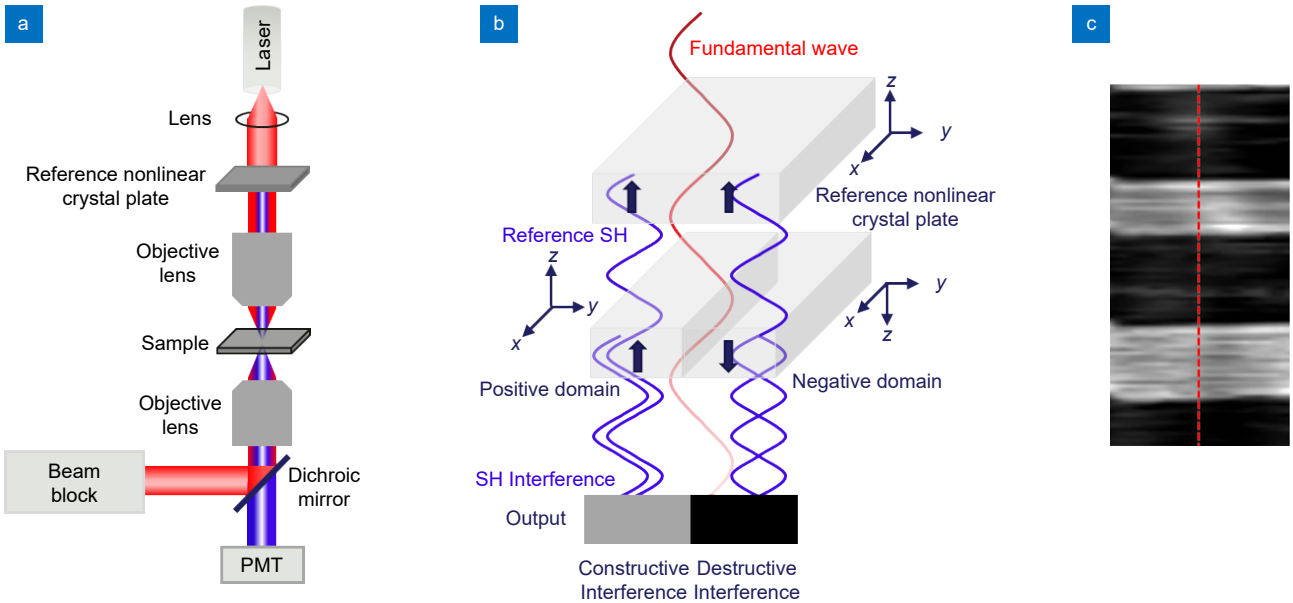

Fig. 5 | (**a**) Schematic of transmission interference SHG microscopy. (**b**) Illustration of interference process that is used for imaging the domain pattern, redrawn from ref.[53], IOP Publishing. (**c**) Example of an interference SHG microscopy image of a periodically poled LN crystal. Figure reproduced with permission from ref.[54], Optical Society of America.

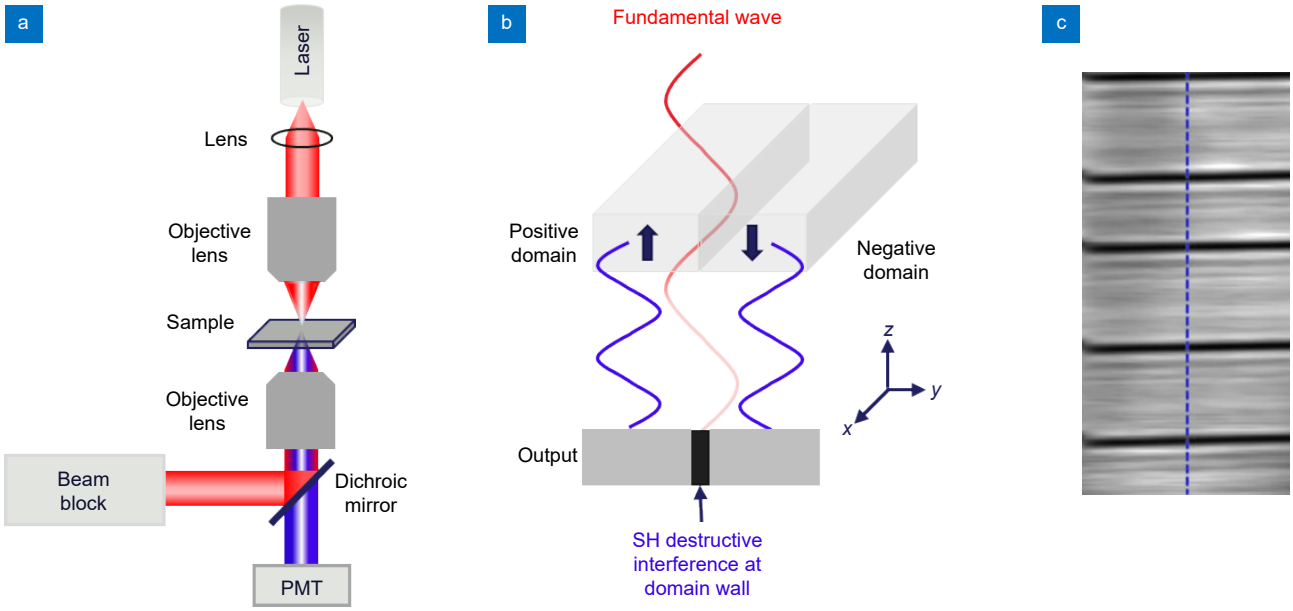

Fig. 6 | (**a**) Schematic of transmission non-interference SHG microscopy. (**b**) Illustration of interference of SH signals at the domain boundary, causing the disappearance of the SH signal. (**c**) Example of a non-interference SHG microscopy image of a periodically poled LN crystal. Figure reproduced with permission from ref.[54], Optical Society of America.

ferroelectric domain wall in LN. This drop in the SH signal is suspected to be due to the lower value of the second-order nonlinear coefficients caused by twisted crystal structure near the boundaries[53]. Recent SH investigation also revealed that ferroelectric domain walls in LN give rise to new, rotated tensor elements with induced strain[51], and such distortions in crystal structure and symmetry in the vicinity give rise to a different SH intensity response[56,57]. The reduced SH signal can, therefore, be used to image domain walls, which separate opposing polarized areas in LN crystals.

In Cherenkov SHG microscopy[58–62] a non-collinear SH beam that propagates conically at an angle determined by longitudinal phase matching (see Fig. 7(c)) is used for

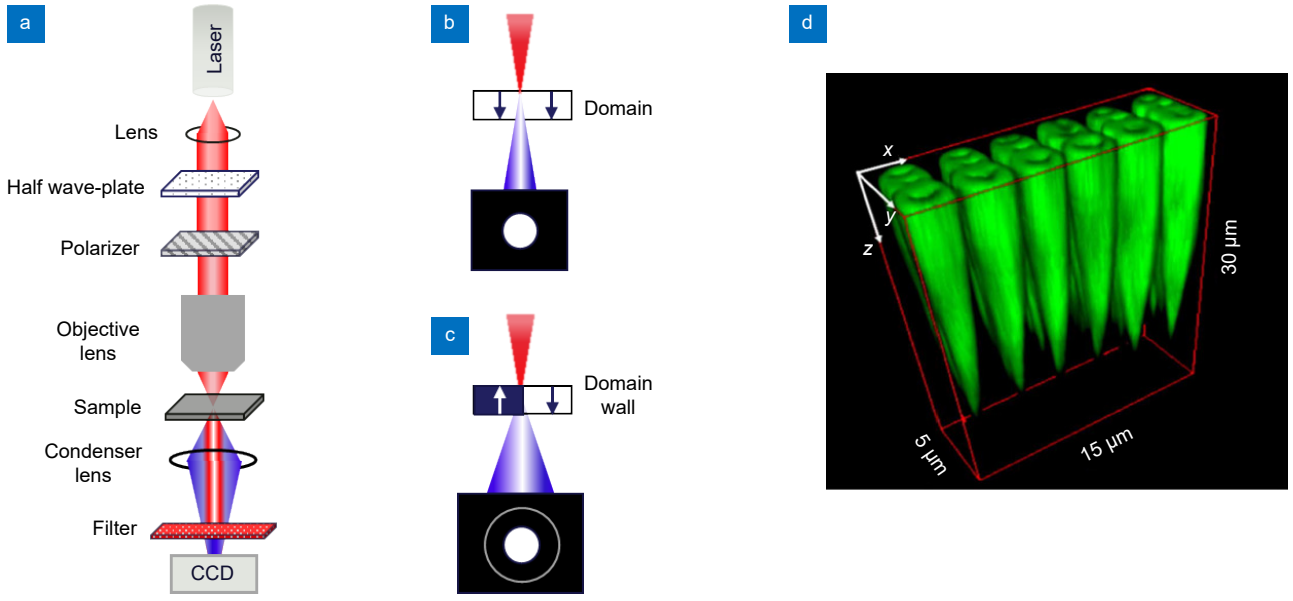

Fig. 7 | (**a**) Schematic of Cerenkov second harmonic generation microscopy. (**b**) Only a collinear (forward) second harmonic signal is generated in a homogeneous sample. (**c**) a conical Cerenkov signal is generated when ferroelectric domain walls are present. (**d**) Three-dimensional visualization of a square pattern of inverted domains by Cerenkov second harmonic microscopy[58]. Figure reproduced with permission from ref.[63], Optical Society of America.

imaging domain walls. This conical SH signal is known as Cherenkov SHG, which is only generated when there is a spatially modulated nonlinear susceptibility, i.e., a ferroelectric domain wall[59,61]. An example of imaged domain walls using Cherenkov SHG can be seen in Fig. 7(d)[59]. The 3D domain imaging is achieved by stacking *X*-*Y* scans recorded at different depths inside the medium[60].

Non-interference microscopy images reveal domain boundaries as dark lines. In contrast, interference microscopy offers polarity distribution with phase information, clearly distinguishing opposite domains as bright and dark areas[53,54]. While both methods offer comparable image resolution, interference microscopy requires additional optical elements. Cherenkov microscopy, however, can offer more detailed insights into domains deep within the crystal through 3D imaging, though it may require specialized equipment[60]. SHG microscopy is an attractive method for imaging domain patterns in LN as it offers non-destructive, high-resolution imaging even in 3 dimensions. However, it should be noted that specialized equipment is required for this imaging method and that the serial scanning process in three dimensions can be time-consuming. This domain pattern imaging technique can be used to visualize domain patterns in bulk LN crystals and in thin-film LNOI. In thin-film LNOI, this method can also provide information about the depth of the inverted domains by analyzing the intensity distribution of the reflected SH signal, which is phase matched in co-propagation[51]. Further, the two-dimensional laser scanning approach compatible with the first two methods would allow faster imaging of a large sample area, enabling easy characterization of domain uniformity, such as variations in domain duty cycle over the length of a long periodically poled crystal/waveguide.

Electro-optic imaging microscopy and polarization microscopy

Electro-optic imaging microscopy is a simple and fast method to image ferroelectric domains nondestructively and in-situ, which has been used for more than half a century. In this technique, the LN sample is placed in a transparent holder that allows the application of an external electric field to the LN crystal via a transparent conducting liquid, such as saturated KNO_3 solution or saturated LiCl solution. A typical setup is illustrated in Fig. 8(a). When an external electric field is applied to the LN crystal, the refractive index of the LN changes depending on the crystal's polarization, caused by the tensorial nature of the electro-optic effect. This causes the refractive index to increase in one domain while it decreases in the opposing polarized domain, creating a refractive index contrast at the domain wall. The index contrast at the domain wall causes scattering of the transmitted light, which can be used to image the domain wall when the crystal holder is placed in an optical microscopy setup[64,65]. This domain visualization technique can also be used to image domain walls after domain reversal without applying an external electric field. A condition for this to work is that the domain inversion process occurs at low temperatures, close to room temperature. In this case, the internal field in LN is sufficiently strong to cause a refractive index difference between opposing polarized domains due to the electro-optic effect. The refractive index difference at the domain wall causes scattering of the transmitted light[66].

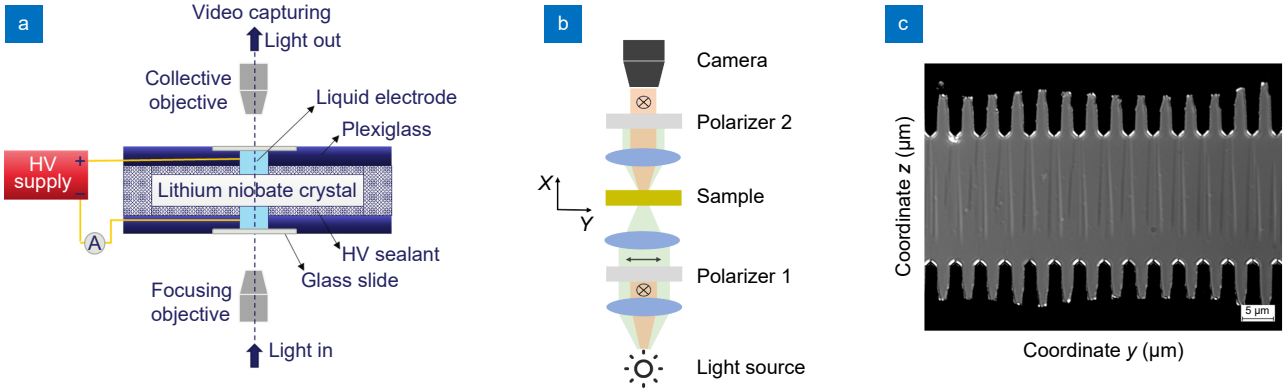

Fig. 8 | (**a**) Schematic of the electro-optic imaging microscopy setup. (**b**) Optical setup with cross polarizers to inspect the poled domains. (**c**) Microscope Image of poled domains analyzed using polarization contract microscopy on an *X*-cut 600 nm thin film LNOI with an LN substrate. Figure redawn from: (a) ref.[64], AIP Publishing; (b) ref.ref.[67], Optical Society of America.

Annealing the poled LN crystal removes the internal field and refractive index difference between domains.

It is also common to add cross-polarizers to the optical setup to form a polarization microscope, as illustrated in Fig. 8(b). Adding cross polarizers can help to increase the contrast and, therefore, improve the imaging quality[64,67]. While the electro-optic imaging microscopy and polarization microscopy techniques are suitable for visualizing domain patterns, as shown in Fig. 8(c), the resolution of this domain visualization method is diffraction limited[46]. Furthermore, it should be noted that both approaches are applied in transmission mode, which requires transparent samples such as bulk LN wafers or thin-film LNOI samples with a silica buffer and LN handle (substrate), as shown in Fig. 8(c).

Summary of the domain visualization methods

In the previous sections, a brief overview of some of the most commonly used domain visualization methods was provided, including selective chemical etching, piezoresponse force microscopy, second harmonic generation (SHG) microscopy, electro-optic imaging microscopy, and polarization microscopy. While each method has advantages and disadvantages, in recent years, the SHG microscopy approach has widely been opted for visualizing domains in the micrometer range due to its non-destructive, good image resolution, and quick imaging attributes. This enables more flexibility in the domain engineering and fabrication of periodically poled waveguides. In the following table, we provide a brief comparison of these domain visualization methods.

Domain engineering methods

In 1962 Armstrong et al.[68] proposed a theory for improving the nonlinear optical process of the second harmonic generation by using stacks of crystals, where the crystals have alternating orientations of the spontaneous polarization. While this can be achieved by carefully stacking many crystal sheets, it soon became unpractical due to the many interface reflections, the large number of crystals and the fragile thin crystal sheets. This motivated the search for alternative methods to achieve spatial control over the crystal's spontaneous polarization, giving birth to the field of domain engineering.

Over time numerous methods have been developed to invert the spontaneous polarization of LN. In the 1960s, single crystal LN was grown by Czochralski technique[2,3,68,69], which shortly afterwards provided the means to grow LN crystals with control over the direction of LN's spontaneous polarization by using a temperature gradient at the crystal-melt interface during the crystal growth. This control enabled the creation of tailored domain patterns during the crystal growth process[3,70]. In the 1980s, post-growth domain inversion was discovered caused by the diffusion of defects and/or dopants in LN, examples include LiO_2 out-diffusion[71] and Ti in-diffusion[72]. A breakthrough in the domain engineering of LN occurred in the 1990's when Yamada et al.[17] discovered that applying a strong electric field along the polar Z-axis of LN crystal can cause domain inversion at room temperature, thereby establishing a more convenient domain engineering method. This domain engineering method is also often termed 'Electric Field

Table 1 | Comparison of visualization techniques.

Visualization technique	Advantage	Disadvantage
Selective chemical etching	• No sophisticated equipment required. • Large areas can be imaged quickly. • High resolution images possible when combined with SEM.	• Invasive process that alters the surface of LN. Can be destructive if the sample's surface quality is important. • Mainly 2D information of the domain can be recorded by this technique.
Piezoresponse force microscope	• Non-invasive technique. • Features of nanometers can be measured.	• Serial process, not ideal for imaging large areas. • Mainly 2D information of the domain can be recorded by this technique. • Specialized equipment required.
Second harmonic generation microscopy	• Non-invasive technique. • In-situ domain visualization possible. • 3D visualization of domains possible. • Quick 2D large area imaging through laser scanning with good spatial resolution (~0.5–1 μm)[49]	• 3D visualization is time consuming, but 2D visualization is relatively quick. • Specialized equipment required.
Electro-optic imaging and polarization microscopy	• Non-invasive technique. • In-situ visualization of domain possible. • Large areas can be imaged quickly.	• Comparatively low-resolution images.

Poling' and is the most widely used domain inversion method for LN. However, the requirement to achieve high spatial resolution and good control over the domain growth has motivated the search for other domain engineering methods such as atomic force microscopy (AFM), light assisted poling (LAP), electron or ion beam bombardment, direct laser writing, and 3D femtosecond laser writing. The following sections provide an overview of some of the most used domain engineering methods for bulk LN and thin-film LNOI.

Temperature mediated poling

When LN was first grown by the Czochralski or Bridgeman technique, the crystals had multi domains and the domain formation could not be controlled. To overcome this challenge Nassau et al.[3,70] introduced three techniques of Czochralski growth to achieve single crystal and single domain LN crystals: (i) applying a weak external electric field during growth (see Fig. 9(a)), (ii) applying a weak external field during the reheating process and (iii) by introducing impurities like MoO_3[3,70], Yt[73], MgO[74], Cr[75], etc. into the melt mixture. In techniques (i) and (ii), the applied external electric field during the cooling phase (as the crystal transitions from the paraelectric state (above the Curie temperature) to the ferroelectric state (below the Curie temperature)) ensures the orientation of the crystal polarization. This is the case, as the applied electric field is higher than the coercive electric field at crystal temperatures just below the Curie temperature, resulting in single crystal and single domain LN crystals. In technique (iii) no external electric field is applied to the crystal, here the impurities gradient at the growth boundaries causes an electrically charged layer, and this internal electric field can be higher than the coercive electric field at temperatures just below the Curie temperature, enabling the growth of single

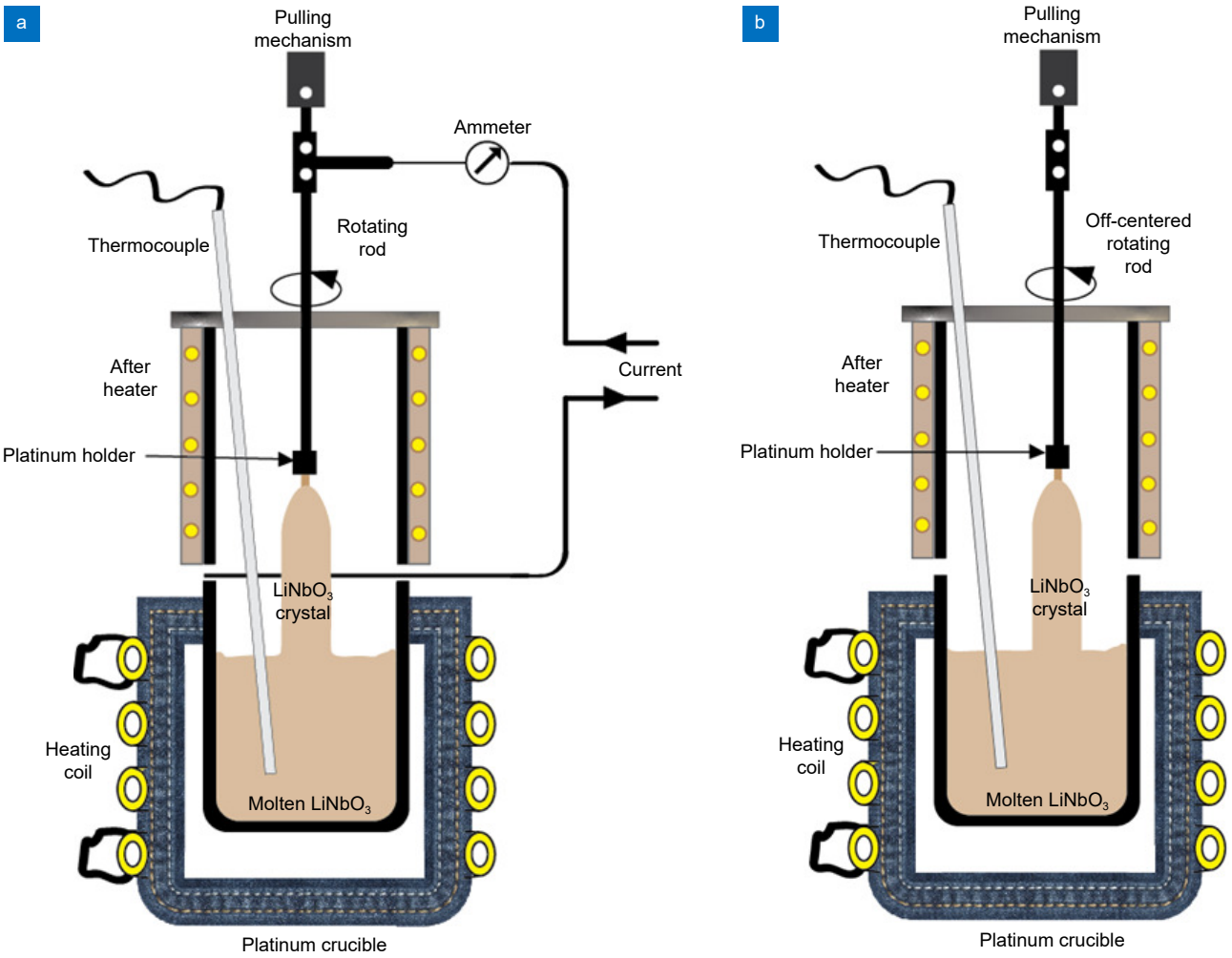

Fig. 9 | Schematic of (**a**) single crystal and single domain Czochralski growth technique by applying electric field redrawn from ref.[3], and (**b**) off-centered Czochralski growth technique for PPLN.

crystal and single domain LN crystals.

It has been shown that by modifying the above techniques, one can achieve periodically poled LN crystals[76]. For example, when using the technique (i) in which an electric field is applied during growth, one can obtain periodic domains in LN crystals by periodically reversing the direction of the applied external electric field during the growth process. The spatial period of the inverted domain depends on the pull/growth rate and the square wave frequency of the applied electric field.

Modifying the single domain growth technique by placing the crystal's growth axis (rotational axis) asymmetrically to the temperature field can also generate periodically poled LN crystals. This growth technique is also known as off-center Czochralski growth and is illustrated in Fig. 9(b). The asymmetrically placed growth axis of the crystal causes periodic inversion of crystal polarization due to the periodic change in the temperature gradient, growth rotation and impurity concentration, which cause a periodic change of the internal electric fields[73,74,77,78]. The period of the inverted domain is controlled by the pull/growth rate and the rotation speed.

One of the drawbacks of the introduced methods to generate periodically poled LN crystals is the variation of the inverted domain period. However, these domain engineering methods are attractive for the mass production of bulk periodically poled LN crystals with larger periods, particularly for crystals thicker than 1 mm. Periodically poled LN crystals grown by the above methods were successfully used for nonlinear optical applications using quasi-phase matching (QPM)[75,79]. The feasibility of applying this technique for domain patterning LNOI could be in using the poled bulk crystals for the ion-slicing process[80] for the mass manufacturing of periodically poled LNOI wafers.

Defect diffusion

In the previous section, it was mentioned that an impurity or defect gradient can induce an internal electric field, which can be used to control the spontaneous polarization of the LN crystal when it is grown out of the melt. In this section domain engineering methods are introduced that also rely on an internal electric field that is generated by defect gradients, however this time on a sample or wafer level. The defect gradient is generated by carefully controlling the environment of the LN crystal and heating the crystal to elevated temperatures to drive the diffusion process and reduce the coercive field of the LN crystal. In the following an overview is given for domain inversion by (i) Li_2O out-diffusion and (ii) Ti in-diffusion.

Domain inversion by Li_2O out-diffusion was first observed by Nakamura et al.[71,81]. They discovered that subjecting LN crystals to temperatures above 1070 °C in an air or argon gas environment for an extended time period results in domain inversion of up to half of the LN thickness due to Li_2O out-diffusion. The domain inversion process starts from the $+Z$ face of the crystal. The thickness of the inverted domains depends on parameters such as temperature, heat treatment duration, cooling time, and gas atmosphere[81,82]. Later, Rosenman et al.[82,83] demonstrated that domain inversion can be controlled by modifying the boundary conditions of the out-diffusion process. They achieved this control by pressing LN crystal's $-Z$ faces against each other, creating an asymmetric out-diffusion condition.

Doping LN with metals like Titanium (Ti) is a widely employed method for generating refractive index contrast for optical waveguides in LN crystals. Miyazawa[72] demonstrated that this process can also be utilized to induce domain inversion in LN. A schematic illustration of the process flow is shown in Fig. 10. In this technique, a Ti layer is deposited on the $+Z$ face of the LN crystal, which is then heated in a furnace with airflow for 5-10 hours at temperatures of ~1000 °C, followed by a gradual cooling to room temperature. Using this method, domains with thicknesses of up to 10 μm have been demonstrated[72]. Miyazawa and Thaniyavarn showed that domain formation by Ti-diffusion is dependent on the Ti concentration, diffusion temperature, and time[72,84–86]. This domain engineering technique is barely used nowadays as the generated domain can suffer from microdomain formation in the crystal, which can cause optical diffraction, and the electro-optic properties of the crystal can also be degraded[72].

Domain engineering by using defect diffusion has been demonstrated in bulk LN crystals. It has yet to be seen if it is feasible to use this technique in thin-film LNOI, due to the high temperatures that are required in the process. Furthermore, other domain engineering methods may provide better control over the domain formation process in thin-film LNOI.

Electric field poling

Electric field poling is arguably the most commonly used method for domain engineering LN. One can

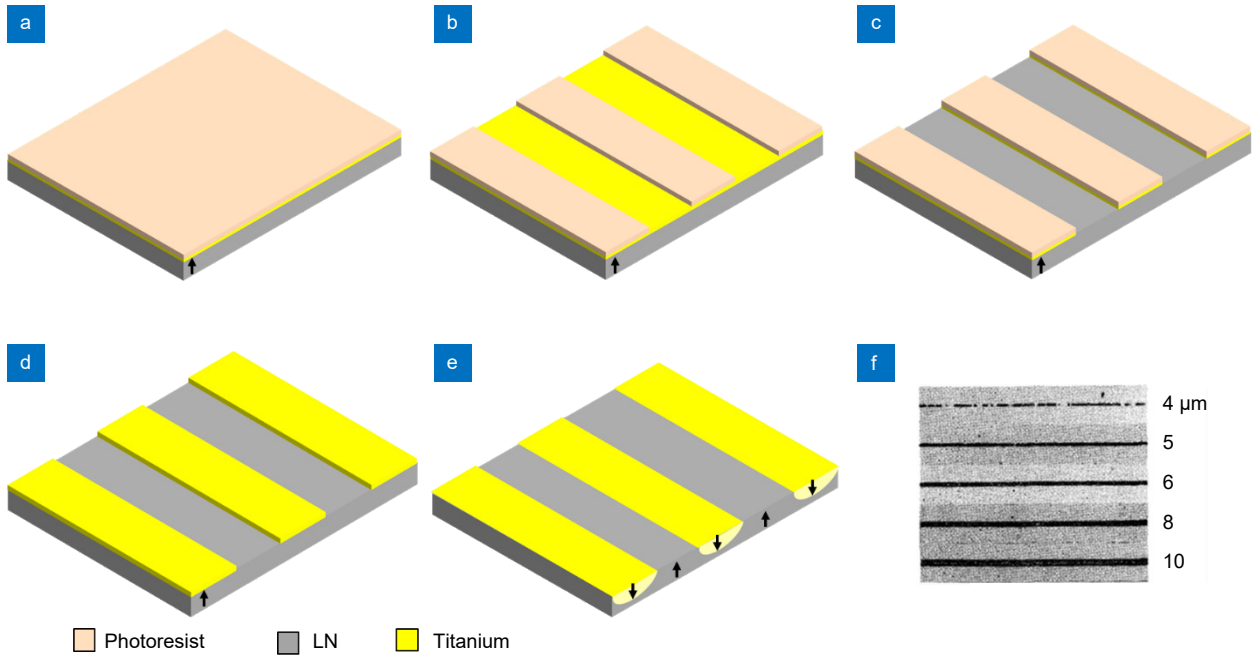

Fig. 10 | (**a**) Evaporation of metallic titanium and spin coating of photoresist, (**b**) patterning and development of resist, (**c**) wet etching of titanium, (**d**) removal of photoresist, (**e**) titanium indiffusion by heating in a furnace and domain inversion, and (**f**) etched-surface micrograph of inverted domains. Figure reproduced with permission from ref.[72], AIP Publishing.

distinguish different methods of electric field poling; however, they have in common that an external electric field, higher than the coercive electric field of LN, is applied to the crystal, causing domain inversion at room temperature. The strong external electric field required for inverting domains in LN crystal can be generated by different methods, such as (i) by applying an electrical potential difference between a pair of patterned electrodes on the surface of LN crystals, (ii) by applying a potential difference between a tip of an atomic force microscope and a surface electrode on LN crystals or (iii) by depositing charges on the LN crystal surface by using an electron or ion beam. The following sections describe the three electric field poling methods in more detail.

Patterned surface electrodes poling

In bulk LN, *Z*-cut is the most common crystal cut used for electric field poling with patterned surface electrodes. The preference for this cut can be explained by the ease of placement of the patterned surface electrodes on the polar faces of the crystal (see Fig. 11(a)), allowing the application of an electric field along the polar *Z*-axis. Two types of electrodes are commonly used for electric field poling: (i) patterned metal electrodes (see Fig. 11)[17] and (ii) liquid electrodes (such as a LiCl solution)[87], which use a patterned photoresist as an electrically insulating layer to define the desired poling pattern[88]. In both cases, a high potential difference is applied to the electrodes, creating a strong electric field, which causes localized domain inversion when the applied field is above the coercive field strength of the crystal (e.g., in bulk CLN, the coercive field is ~21 kV/mm). The first stage in domain formation is nucleation, where each individual domain has a single starting point called the nucleation site[89]. Nucleation occurs exclusively at the electrodes and the nucleation sites are typically concentrated along the edges, as illustrated in Fig. 11(a), caused by the higher electric field strength at the electrode edge. Furthermore, the domain nucleation sites are more pronounced at the positive electrode. The nucleated domains propagate along the polar axis to the other side of the LN crystal and terminate at the ground electrode, as illustrated in Fig. 11(b) and 11(c). Afterwards, the narrow domains coalesce underneath the electrode (Fig. 11(d)) and continue to laterally expand (Fig. 11(e)), which can cause the merging of the domains if the domain inversion process is not stopped by reducing the applied electric field.

Various parameters impact the promotion of new nucleation sites and the growth of the domains. These include voltage strength, pulse duration, number of pulses, and rest time between each pulse. Generally, domains tend to grow more quickly with an increase in voltage

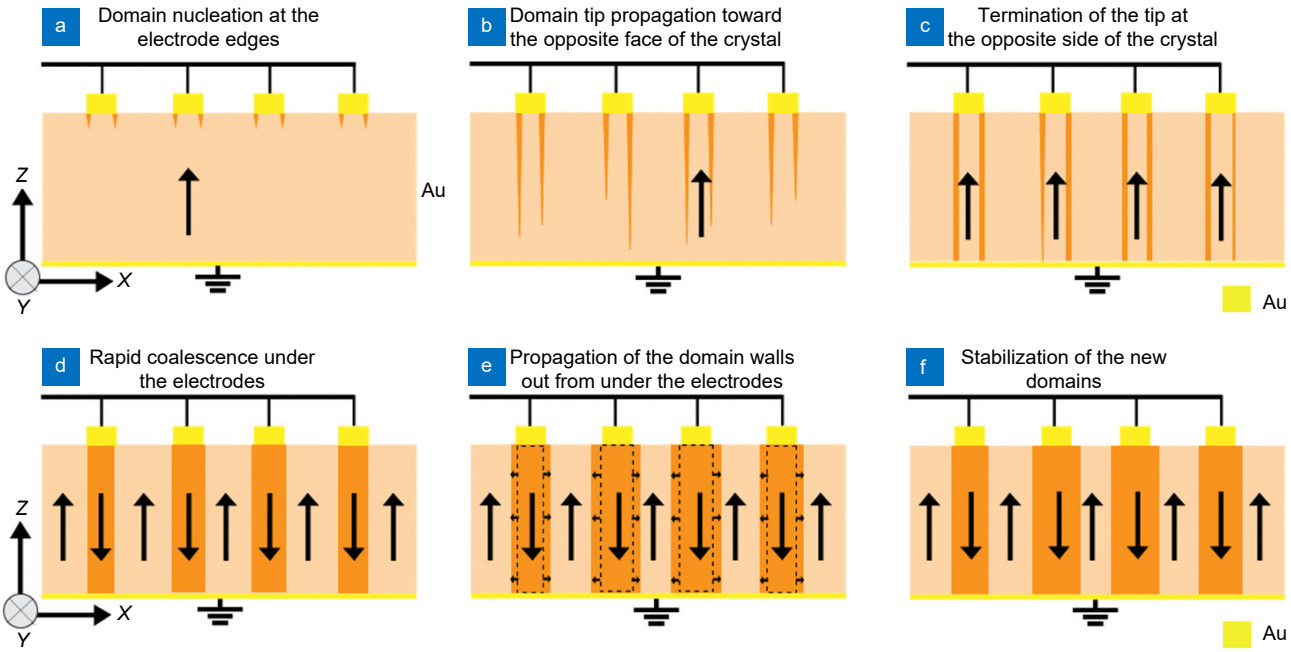

Fig. 11 | Illustration of the six stages of domain kinetics during electric field periodic poling. (**a**) Domain nucleation at the electrode edges. (**b**) Domain tip propagation toward the opposite face of the crystal. (**c**) Termination of the domain tips at the opposite side of the crystal. (**d**) Rapid coalescence under the electrodes. (**e**) Lateral domain growth. (**f**) Stabilization of the inverted domains. Illustration redrawn from ref.[89].

and continue the domain growth process and lateral expansion (Fig. 11(e)) for longer pulse durations. Hence, optimizing the strength and duration of the voltage applied to the electrodes to control the domain growth is essential. One of the biggest challenges in domain patterning of bulk LN is suppressing lateral domain expansion while achieving uniform in-depth inversion, particularly for short domain periods (<4 μm) when a standard LN crystal thickness of 500 μm is used[90,91]. In general, one can distinguish between two different electric field poling strategies, one is the application of a single pulse above the coercive field to initiate nucleation and domain growth, followed by a voltage value below the threshold limit for domain stabilization, and the other is the application of multiple short voltage pulses above the coercive field to achieve uniform domain patterns[92]. In the case that pulses are used, a time delay is applied between the pulses to reduce the heating of the crystal, which can cause undesired lateral domain expansion[57,93]. With careful control over these supply parameters, this domain engineering method allows the fabrication of uniform domain patterns with a duty cycle close to the desired value with high repeatability[89].

In thin-film LNOI, the approach to achieve domain inversion with patterned electrodes is similar to that of bulk LN. One difference is that *X*-cut LNOI (see Fig. 12(l)) is more commonly used as the poling electrodes can be applied in a single fabrication step. It also allows TE-guided modes in the patterned waveguide, utilizing LN's strongest non-linear coefficient (d_{33} = 26 pm/V)[94]. For the poling process, comb-shaped electrodes are patterned on the thin-film LNOI surface, which are used to apply electric field pulses along the polar *Z*-axis, causing domain nucleation at the positive tips of the comb electrode. The nucleated domain then grows toward the ground electrode, as illustrated in Fig. 12(a–d), when applied with a single long poling pulse. A similar poling approach can also be used for *Z*-cut LNOI (see Fig. 12(m)), with patterned electrodes located on the top surface for the application of the high voltage signal and an unpatterned electrode underneath the LN layer acting as the ground. The unpatterned electrode can be on the silicon substrate wafer, which has sufficient conductivity. Typically, the LNOI sample is placed on top of a conductive plate (such as Aluminium or Copper), acting as the electrical ground. Conducting the poling process at elevated temperatures (~300° C) can benefit the domain growth process as trapped charges at the LN-SiO_2 interface can more readily be neutralized[22,95]. Another approach to avoid heating during poling involves evaporating a conductive thin film to form an interjacent electrode between the LN thin film and the substrate[45,47]. This

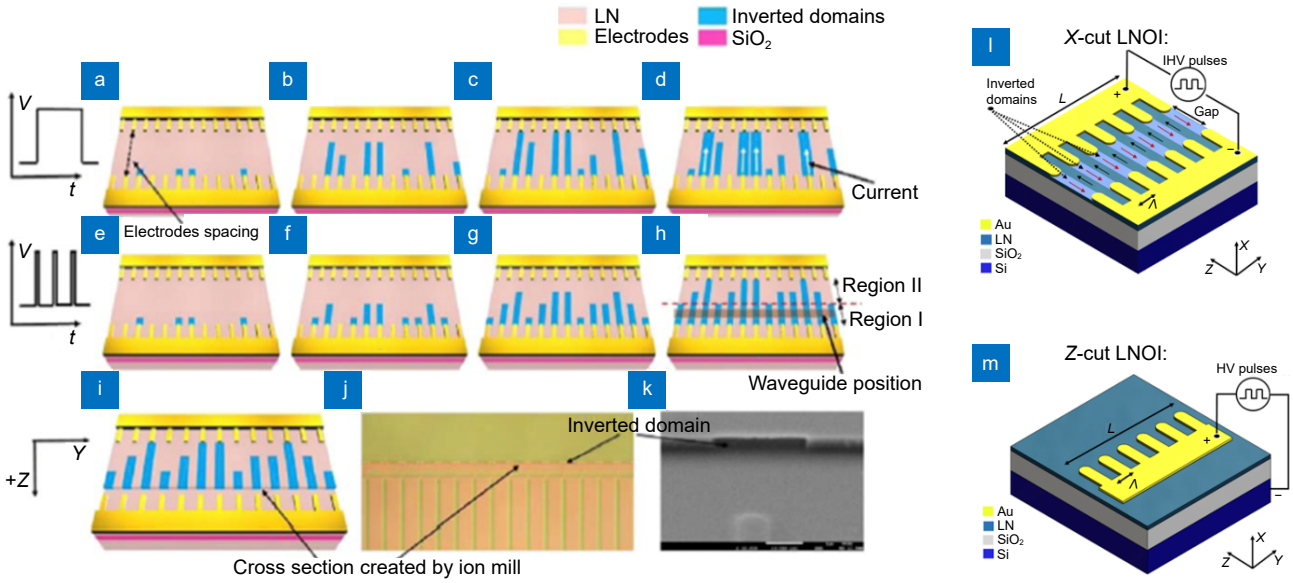

Fig. 12 | (**a–d**) Schematic illustration of the evolution of inverted domain using a single long poling pulse. (**e–h**) Schematic illustration of the evolution of inverted domains using multi-pulse waveforms with short pulse durations. (**i**) Schematic of cross section of the device obtained after ion milling to visualize the periodically poled region. (**j**) Top-view micrograph of the cross section of a poled device after 10 min 48% HF etch at room temperature. The dashed line corresponds to the cross section in which the bright part is the poled area. (**k**) SEM image of inverted domain. (**l**) Schematic illustration of poling process in *X*-cut LNOI. (**m**) Schematic illustration of poling process in *Z*-cut LNOI. Figure reproduced with permission from (a–k) ref [92], Optical Society of America.

conductive electrode film can be short-circuited with the ground electrode. At the same time, the HV supply is applied to the patterned surface electrodes, where the domain can grow from the top surface and terminate at the ground interjacent electrode.

Similar to bulk LN, the domain nucleation and growth in thin-film LNOI strongly depend on supply parameters such as the applied voltage, pulse duration, rest time, and electrode shape/material. The impact of these supply parameters on domain expansion follows a similar fashion. It is important to note that the coercive field in thin-film LNOI is comparatively higher (30 kV/mm) than in bulk LN crystals, which might be caused by the bonding interface between the thin-film LN and silica buffer layer, hindering domain inversion[92]. Several studies of domain inversion in *X*-cut LNOI showed that the shape of the electrode (e.g., utilizing a rounded electrode tip or a sharp electrode tip) can be used to increase and tailor the electric field at the electrode tip, which is an additional degree of freedom difficult to realize in *Z*-cut bulk LN or thin-film LNOI[93]. Since the length of the inverted domain in thin-film LN is in the order of tens of microns, a series of comparatively short pulses are commonly used to achieve uniform domain nucleation, resulting in better uniformity of the domain pattern in LNOI (see Fig. 12(e–h)). The shorter length of the inverted domains in thin-film LNOI also allows for the fabrication of sub-micron domain periods[96], which is much more challenging in bulk LN.

Additionally, in nonlinear processes like second harmonic generation, uniform domains with a duty cycle close to 50% are crucial for efficient phase matching[97]. Hence, excellent control over the domain dimensions is desired, which is typically challenging due to the semi-random domain nucleation and growth process, as highlighted in this section above. This often requires process optimization from wafer to wafer, which involves quantifying and understanding different variables defining domain evolution. The real-time domain visualization during electric field poling can make the optimization process more flexible and dynamic, thereby enabling a robust fabrication process with enhanced consistency.

Atomic force microscopy poling

Atomic force microscopy (AFM) poling enables the 'writing' of sub-micron-sized inverted domains and was first demonstrated in bulk LN[98,99], as illustrated in Fig. 13(a). This domain inversion method is typically applied to *Z*-cut LN crystals, where the backside of the LN crystal is connected to the electrical ground and voltage

pulses are applied to the tip of the AFM, which is moved along the top LN surface. Domain inversion occurs when the electrical field is higher than the coercive field of LN. It is important to note that the sharp tip of the AFM enhances the electric field, resulting in a strong electric field even when moderate voltages are used. However, the poling of thick LN crystals (e.g., 500 μm) is challenging as the electric field strength decreases quickly with distance from the AFM tip.

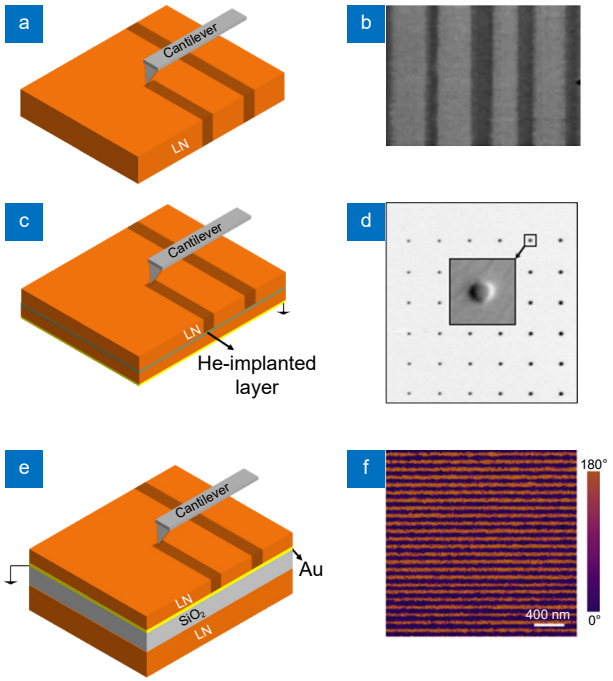

Fig. 13 | Schematic illustration of the AFM-tip domain writing process for (**a**) bulk LN; (**c**) helium implanted bulk LN; and (**e**) thin-film LNOI. (**b**) Electrostatic force microscopy image of inverted domains in Bulk LN. (**d**) PFM image of inverted domains in He-implanted bulk LN. (**f**) PFM image of inverted domains in thin-film LNOI. Figure reproduced with permission from: (b) ref.[98], (d) ref.[100], AIP Publishing; ref.[102], Optical Society of America.

A method to avoid the need to domain invert the entire wafer thickness is to use helium (He) implanted LN crystals, as illustrated in Fig. 13(c). The helium ions are implanted into the LN with depths of tens of microns[100], creating a defect layer within that LN crystal at which inverted domains from the AFM writing process are 'pinned', allowing the energetically unfavorable state of opposing crystal polarization within the crystal. However, the pinning of the domain in the crystal can also result in trapped charges, which can hinder the domain inversion in the proximity of already inverted domains. This can manifest in a series of inverted domain dots, rather than an inverted line when the AFM tip is scanned across the surface[101].

Using thin-film LNOI instead of bulk LN provides three major advantages to the AFM domain writing process, (i) the LN film is naturally thin, so the whole thickness of the LN can be inverted with no opposing crystal polarization or trapped charges, (ii) the applied voltage is significantly reduced due to the reduced LN thickness, and (iii) the electrode can be brought in direct contact or in very close proximity of the LN film improving the electric field profile of the AFM tip. As the trapping of charges is strongly alleviated, writing of continuous domain lines with very high resolution is possible, providing the means to achieve periodic domain structure with periods of 100 nm and a duty cycle close to 50%[102], as shown in Fig. 13(f). Gainutdinov[103], Guang-hao[104], Agronin[99], Volk[105] give an excellent explanation and overview of AFM poling methods, where they investigated various LN thin-film thickness, applied voltage, duration of the pulse, and stability of inverted domains. One of the most discussed disadvantages of AFM is the time required to write these domains (serial process) and stitching errors in case domain patterns larger than the writing field are required.

Nevertheless, this domain writing method is a powerful method to achieve sub-micron-sized domains in bulk LN and thin-film LNOI crystals. The width of inverted domains can be controlled by the duration of the pulse and the applied voltage to the AFM tip, while the depth can be controlled by the He implantation depth or LN crystal thickness. This technique has recently shown the capability to generate reliable, repeatable submicron domains in *X*-cut LNOI[48,106].

Electron and ion beam poling

Rather than using electrodes to apply an electric field to the LN crystal to invert the spontaneous polarization, one can also 'deposit' charge carriers such as electrons or ions on the surface of the LN crystal. In both processes, the deposition of charge carriers is conducted in a vacuum to enable the accumulation of the charges on the LN surface, generating a strong electric field. If the electric field is higher than the coercive field of LN, it can cause domain inversion[107,108]. In the following an overview is provided of the electron and ion beam domain inversion processes.

In electron beam poling, a scanning electron microscope (SEM)[109–112] or electron beam lithography

(EBL)[108,113,114] system is used to deposit electrons on the −*Z* face of the crystal. The +*Z* face of crystal is coated with a conductive later, often a metal layer, forming the ground electrode[112,115]. The electron beam parameters that influence the domain inversion process are acceleration voltage (5 kV–25 kV), e-beam current (0.1 nA–3 nA), exposure time (10 ms–2 s) and irradiation area (0.5 μm²)[116]. It is important to note that the acceleration voltage can be chosen to deposit the electrons a few microns deep in the LN surface, which helps suppress charge neutralization. The nucleation of the domains starts near the −*Z* surface of the crystal and extends until the domain reaches the +*Z* surface. It has been observed that the nucleation site can also depend on the metal electrode that is used[112,117]. 500 μm thick LN crystals can be poled with this technique. The resolution of the fabricated domain patterns is typically much lower (domain sizes of several microns) than the resolution of the SEM or EBL systems (tens to hundreds of nanometers), which can be explained by the high charge accumulation and strong backscattering of electrons causing spreading and merging of the domains[115,116]. The lateral expansion of domains can be reduced by using a resist coating, which helps to accumulate charges in the resist region[108,114].

In ion beam poling, the higher mass of ions helps to reduce the charge accumulation and backscattering when compared to the electron beam poling process[118]. 1D and 2D inverted domain patterns have been demonstrated with periods of 1 μm and below[119,120]. In this technique, ions are deposited on the +*Z*-face of the crystal, and the −*Z*-face is coated with a conductive layer, which is connected to the ground. Ions that have been investigated for this domain engineering method include Ga^{+}, Si^{2+}, and Cu^{+}[118,119,121,122]. Like the electron beam poling process, the domain inversion in the ion beam poling technique is governed by the charge, energy, flux, and fluency of the ion beam (For instance, Cu^{+} ion-based poling parameters include energy of ~30 keV, a flux of ~30 mA/cm², and a fluence of ~2×10^{17} ions/cm²)[122], and the lateral expansion of domains can be reduced by coating the +*Z* face with some resist[107]. The typical domain depth for this domain engineering method is tens of microns while providing a sub-micron resolution. It should be noted that electron and ion beam poling methods can be done in *Y*, and *Z*-cut bulk LN crystal[116,120,123]. Ion beam poling can also be done in *Z*-cut LNOI, and periods down to 200 nm with a duty cycle of 33% over 3 mm length are demonstrated[124]. Achieving domain periods below 200 nm was hindered by the merging of the inverted domains due to broadening effects[124]. Ion beam poling is emerging as a promising technique for attaining sub-micron periods for both optical and acoustic applications.

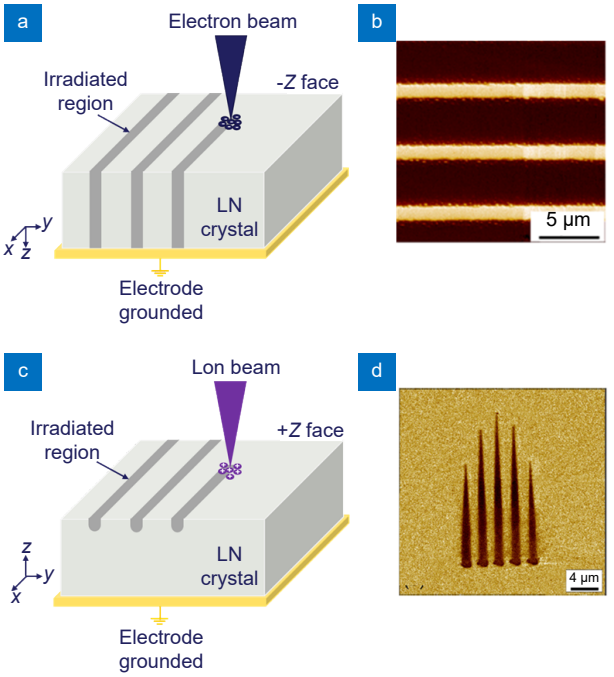

Fig. 14 | Schematic illustration of (**a**) electron beam and (**c**) ion beam poling process, and (**b**, **d**) PFM image of inverted domain[108,120]. Figure reproduced with permission from: (b) ref.[108], AIP Publishing; (d) ref.[120], Taylor & Francis Ltd.

Light-assisted and all optical poling

Light can either assist the poling process, for example, by lowering the coercive field strength, or it can be used to directly invert domains in LN crystals. The various light sources that can be used and flexibility in exposure settings make light assisted and all optical poling methods attractive to achieve high resolution domain patterns. A detailed overview of light-assisted and all optical poling methods can be found in the excellent review by C.Y.J. Ying et al.[125]. In the following, we provide an overview of (i) light-assisted poling, (ii) poling inhibition, (iii) UV laser direct writing and (iv) 3D femtosecond laser writing.

Light-assisted poling

Light-assisted poling makes use of the coercive field reduction of the LN crystals when irradiated with weakly absorbed laser light (e.g., in the visible spectrum). The coercive field is reduced as the weakly absorbing laser light creates a photo-induced space charge field within

the region of interest[28,125,126]. To achieve domain inversion with this method, one needs to apply an electric field to the LN crystal at the same time as the crystal is irradiated with the laser light. This can be achieved by using a setup like the one illustrated in Fig. 15(a), which uses liquid electrodes for applying the uniform electric field. Selective irradiation of the LN crystal results in a localized reduction in the coercive field, and if the coercive field is below the electric field applied to the crystal, domain nucleation and inversion occur. Light-assisted poling removes the need for structured electrodes at the surface of the LN crystal. An example of a domain pattern generated by this poling method can be seen in Fig. 15(b). It should be noted that the reduction of the coercive field strength depends on the LN doping level, the used laser wavelength and if a continuous wave or a pulsed laser light is used. A detailed overview of the experimental investigations can be found in ref.[125–132].

A slight modification of the above poling method is latent light assisted poling. In this process, the irradiation process is decoupled from the application of an electric field, which means that the LN crystal is first irradiated with weakly absorbing laser light, followed by the application of an electric field to the LN crystal, which can occur hours later. This domain inversion process has been demonstrated in congruent LN, while it was not possible to domain engineer Mg doped LN crystals with this method[125,130].

Light-assisted poling and latent light assisted poling have been demonstrated in bulk LN crystals. Applying this technique in LNOI with a transparent substrate would be intriguing, as it could eliminate the need for fine finger electrodes, which are required for sub-micron poling by EFP. It must be seen if these poling methods can be transferred to thin-film LNOI.

Poling inhibition

Poling inhibition is a domain engineering process which is used to create surface domains in LN crystals[133–135]. In this process, continuous wave UV laser light with a photon energy larger than the band gap of LN is focused on the +*Z* face of the LN crystal. The LN crystal is moved with motorized translation stages to enable the irradiation of arbitrary shapes and areas on its surface. The UV laser light is strongly absorbed at the surface of LN, creating a local heating profile, as illustrated in Fig. 16(a). The temperature profile of the localized heating causes an asymmetric diffusion of Li (Fig. 16(b)) from the heated area into the surrounding cooler LN. As the coercive field strength of LN depends on the Li concentration, a coercive field profile is generated in the LN crystal, which has a higher coercive field at the area that was heated by the UV laser light and a lower coercive field around the heated area (Fig. 16(c)). Afterwards a uniform electric field is applied to the LN crystal (Fig. 16(d)) with a field strength higher than the coercive field of LN, but below the coercive field of the previously UV laser irradiated area. This causes domain inversion for the whole crystal except for the previously UV laser irradiated area, resulting in surface domains as illustrated in Fig. 16(f). Poling periods down to 2.9 μm and depths of 1.5 to 4.3 μm have been demonstrated with this method[125].

A few variations on the poling inhibition domain engineering methods have also been investigated. For example, the use of an additional poling step, sometimes referred to as 'reverse' poling, which can be used to achieve bulk domains in Mg doped LN crystals[135] or the use of a silicon layer on top of the LN crystal to enable

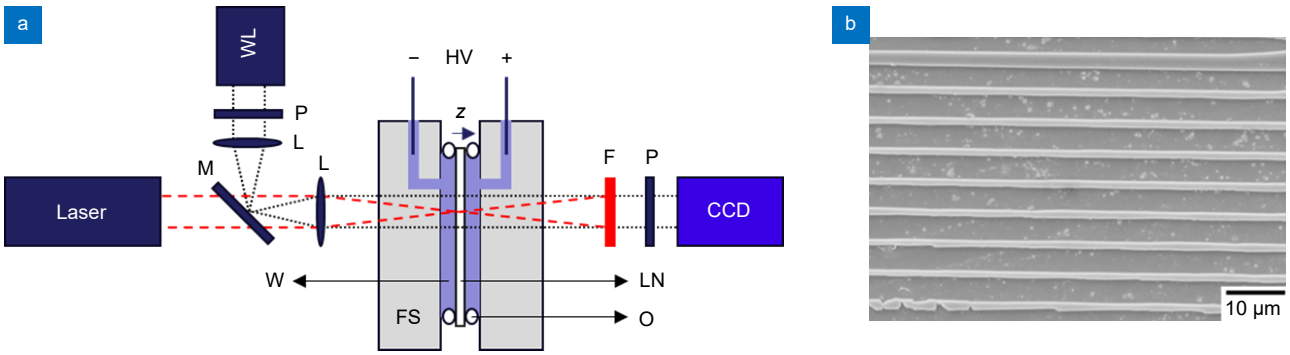

Fig. 15 | (**a**) Schematic of a light-assisted poling setup, showing the focusing of the illuminating laser beam on the +*Z* face of a LN crystal held between liquid electrodes (W) using fused silica (FS) plates, replotted from ref.[131] . The white light (WL) is used only for visualization of the poling process via the crossed polarizer and CCD camera. (P = crossed polarizers; L = lens; F = filter to block the laser beam; M = dielectric mirror; HV = high voltage; O = O-ring). (**b**) SEM image of inverted domains. Figure reproduced with permission from (b) ref.[130], Taylor & Francis Ltd.

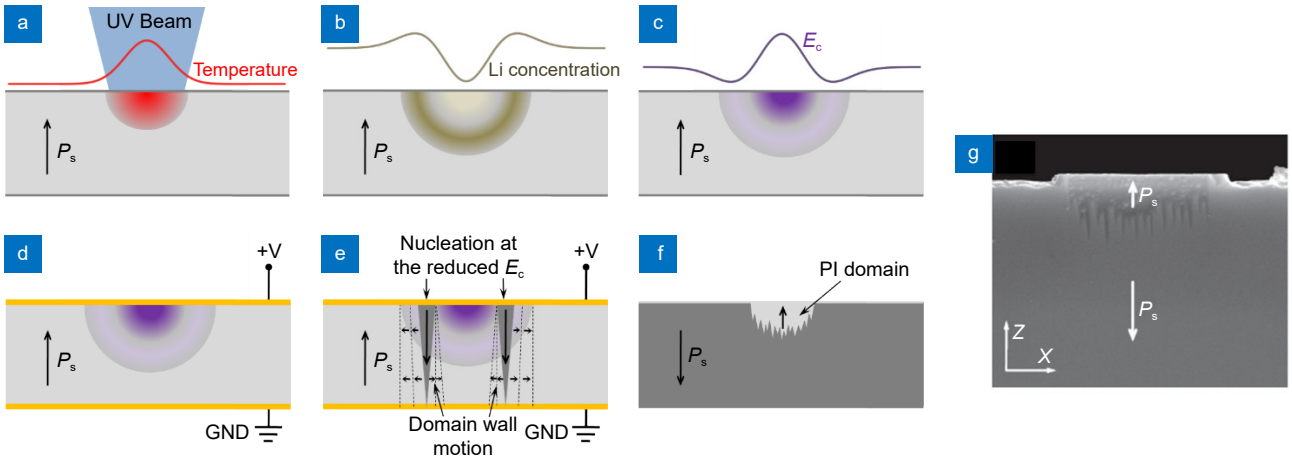

Fig. 16 | Illustration of the poling inhibition process. The focused UV light is strongly absorbed at the crystal surface, generating a local heat profile (**a**), which causes Li diffusion into the colder adjacent crystal (**b**). The coercive depends on the Li concentration (**c**). When a poling step is applied (**d**), the domains prefer to nucleate at the Li enriched region next to the UV-irradiated area (**e**). The Li deficient region on the other hand is poling inhibited, resulting in a surface domain when the poling step is completed (**f**). SEM image of poling inhibited domain cross-section after HF-etching (**g**). Figure reprinted with the permission from (g) ref.[135], AIP Publishing.

the use of visible laser light and the additional benefit of reducing surface damage that can be caused when strongly absorbing UV laser light is used[136]. Domain inversion via poling inhibition has been successfully demonstrated in bulk LN crystals. However, its applicability to LNOI presents challenges due to the elevated temperatures required during the process, which can lead to the delamination of layers in the material stack.

Laser direct writing

Laser direct writing is a domain engineering process that can be used to write surface domains on the $-Z$ face as well as X and Y cut LN crystals[134,137,138]. In contrast to the light-assisted poling and the poling inhibition domain engineering methods, no electric field poling step is required to create inverted domains.

In the laser direct writing process, strongly absorbing laser light (typically UV laser light) is focused on the surface of the LN crystal, which is located on motorized translation stages to allow the focal spot to be scanned across the LN crystal surface. The high absorption of the UV laser light causes localized heating at the surface, resulting in a large temperature gradient, which induces an electric field in the LN crystal of thermoelectric origin. As the coercive field of LN is low at temperatures close to the Curie temperature, the thermoelectric field can be sufficient to cause domain inversion (similar to the temperature mediated poling process described in Section *Temperature mediated poling*). Due to the polarity of the thermoelectric field, it is possible to directly write domains with this method on the $-Z$ face as well as X and Y cut LN crystals. On X and Y-cut LN, it is possible to write and erase domains depending on the scanning direction of the focal spot[134]. Figure 17 shows the illustrative process for the domain inversion depending on different crystal cuts[27,138]. It is important to note that the high temperature gradient generated in this domain engineering method often causes surface damage in the form of cracks, which is undesirable for many applications.

A slight modification of the laser direct writing technique is the use of the Cr layer prior to the irradiation process. The Cr partially absorbs the UV laser light, causing it to heat up and act as an oxygen sink, which in turn causes a defect diffusion gradient at the LN crystal surface[139]. Similar to the defect diffusion domain engineering mechanism described in Section *Defect diffusion*, the defect diffusion gradient caused by the heated Cr layer results in localized domain inversion. As this domain engineering process takes place with slightly lower temperature gradients, the surface damage is reduced when compared to the UV laser direct writing process. However, the reduction of the oxygen concentration causes a reduced transparency of the LN crystal at visible wavelengths.

Visible laser light (e.g., 532 nm) can also be used to irradiate the Cr layer, as it is partially absorbed by the metal. Furthermore, if one uses a Cr pattern, the visible laser light is only absorbed at the Cr coated areas, whereas the uncoated areas transmit or reflect the laser light. This allows for the Cr pattern to be 'imprinted' as an inverted

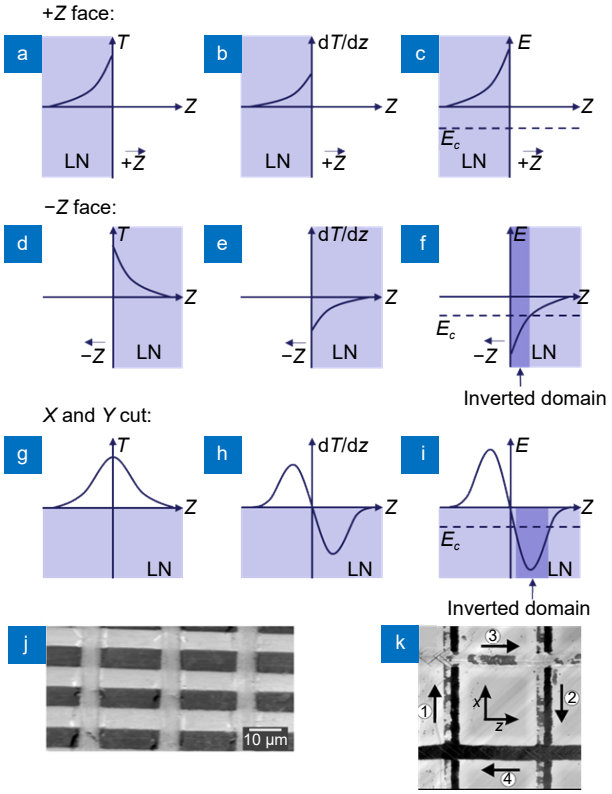

Fig. 17 | Illustration of the laser direct writing process on the +*Z* face (**a**–**c**), −*Z* face (**d**–**f**), and *X* and *Y* cut crystal (**g**–**i**). Domain inversion occurs when the thermoelectric field is higher than the coercive field of the Lithium Niobate (LN) crystal. PFM images of inverted domains on the *Z* face. In the PFM image −*Z* domains appear black and +*Z* domains appear white (**j**) and *Y*-cut[134], where the direction of irradiation is in chronology (1 to 4) (**k**). Figure reproduced with permission from: (j) ref.[137], Optical Society of America; (k) ref.[134], AIP Publishing.

domain pattern into the surface of the LN crystal. The domain inversion process is illustrated in Fig. 18(a–c). The advantage of this process is that the Cr pattern can have fine features (smaller than the diffraction limit of laser wavelength used), which has enabled the experimental demonstration of high-resolution domain patterns, as shown in Fig. 18(d–f)[136,139]. One disadvantage of this domain engineering method is that the domain depth is shallow due to the temperature and diffusion profile.

Domain inversion by direct laser writing has yet to be demonstrated in LNOI. Again, this might be due to the temperatures involved in this process. As the Si substrate in LNOI absorbs light, it potentially generates highly localized heat, leading to delamination. Additionally, reflections from the substrate can lead to less precise domains. The technique's adaptation to LNOI with LN or sapphire as a substrate provides an opportunity.

Femtosecond laser writing

Femtosecond laser writing of the ferroelectric domain can be used to create and erase 3D domain patterns in *X*, *Y*, and *Z*-cut LN crystals[58,140–142]. In this technique as shown in Fig. 19(a), a near-infrared ultra-short laser beam (e.g., 800 nm wavelength, 180 fs pulses and a repetition rate of 76 MHz[59]) is focused into LN using a microscope objective with a high numerical aperture. Domain inversion is caused by the heat generated through multiphoton absorption (two-photon absorption is not feasible due to the insufficient wavelength for band-band two-photon absorption). The tight focusing of the laser beam generates a strong temperature gradient, initiating nucleation when the thermoelectric field surpasses the coercive field. The laser spot is then moved along the +*Z* direction to promote domain growth in this direction[59]. This domain engineering method has allowed the demonstration of repeatable periods down to 500 nm with depths up to 30 μm[141]. The domain inversion process depends on parameters such as the laser wavelength, pulse power, pulse duration, repetition rate, writing speed, and the material properties of the crystal used[58,59,63,142,143]. Noteworthy attributes of this domain engineering method include high precision, rapid writing times, non-contact writing, and the absence of the need for an electrode layer, making it an intriguing domain engineering method and, so far, the only domain engineering method that can generate (Fig. 19(b)) and erase 3D domain patterns in LN crystals[58,141].

Domain inversion using femtosecond laser writing has not yet been demonstrated in LNOI. However, there is potential for adapting the technique to thin-film LNOI, particularly when LN or sapphire substrates are used to reduce reflection and absorption of the laser light by the substrate. Indeed, the tight focusing on a localized point can facilitate the creation and erasure of 3D domains in LNOI[141].

Summary of the domain engineering methods

Domain engineering on the lithium niobate (LN) platform is crucial for enabling efficient nonlinear optical processes, sophisticated quantum information processing, effective electro-optic modulation, and many more applications. In the previous sections, an overview of some of the most commonly used domain inversion methods was provided, which included temperature mediated poling, defect diffusion, patterned surface electrodes poling, atomic force microscopy poling, electron

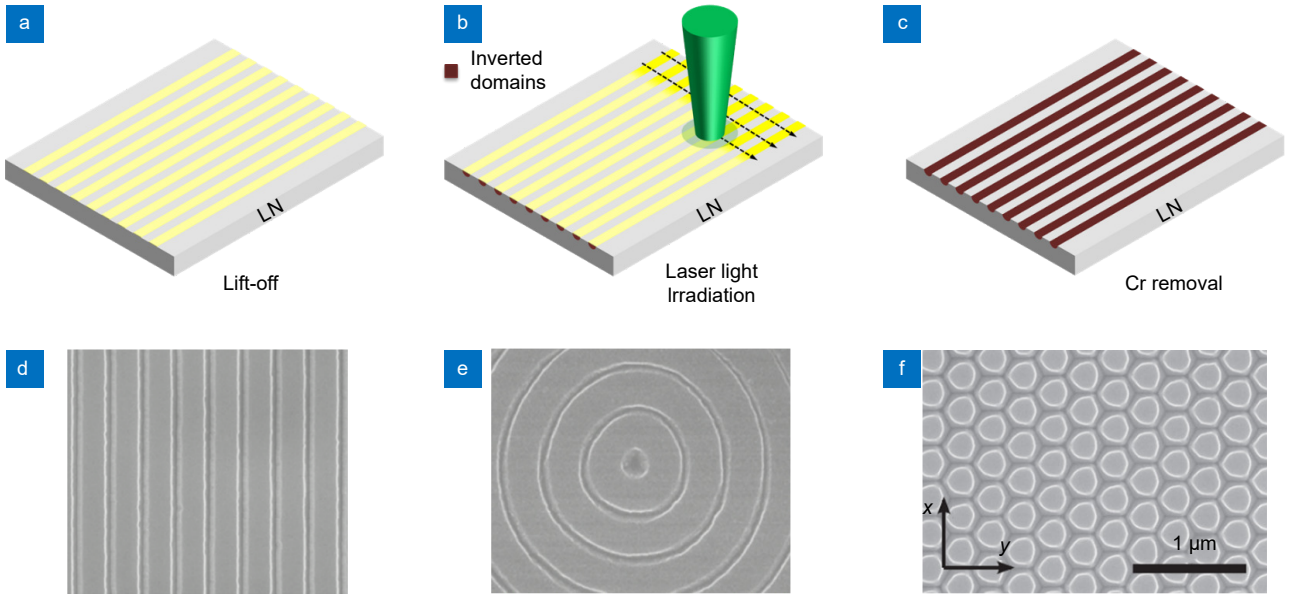

Fig. 18 | Illustration of the fabrication steps for visible light irradiation of a Cr pattern: (**a**) Cr pattern on the surface of a LN crystal, (**b**) generation of the surface domains by laser light irradiation, and (**c**) Cr pattern removal by Cr etchant, and (**d**–**f**) SEM images of domain patterns with period of 300nm. Figure reproduced with permission from (d–f) ref.[139], AIP Publishing.

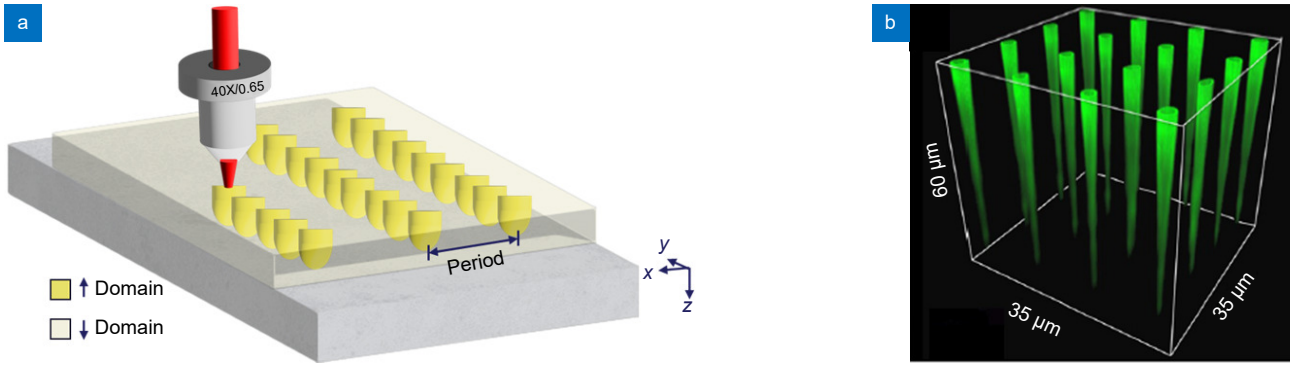

Fig. 19 | (**a**) Schematic of direct writing ferroelectric domain patterns in a LN crystal using femtosecond infrared pulses, and (**b**) 3D profile of inverted domains using Cerenkov second-harmonic microscopy. Figure reproduced from (b) ref.[59], AIP Publishing.

and ion beam poling, light-assisted poling, poling inhibition, laser direct writing, and 3D femtosecond laser writing. In Table 2, we provide a comparison of these domain engineering methods.

In addition to the parameters outlined in Table 2, it should be noted that the uniformity of the inverted domain pattern is a crucial factor for many applications. Techniques like 3D femtosecond laser writing, AFM, electron, or ion beam poling can suffer from stitching errors when the domain pattern is larger than the writing field, which can result in a reduced uniformity of the domain period. In contrast, lithography-based methods such as electric field poling and light-assisted poling experience fewer stitching errors. All domain inversion techniques may encounter random domain nucleation and growth, which influences the uniformity of the duty cycle of the domain pattern.

It is also important to note that poling processes introduce domain walls and potential defects, which may lead to increased scattering losses in waveguides[144], which can affect the overall performance of the device. Besides conventional poling techniques, periodically changing the propagation direction of light, when compared to the LN crystal orientation can also facilitate quasi-phase matching and has been demonstrated in an *X*-cut LNOI microdisk resonator[145]. In this approach, the effective nonlinear optical coefficient oscillates periodically as light propagates around the circumference of the microdisk, avoiding domain inversion processes.

Applications of domain engineered LN

In the previous section, an overview was given for the

different domain engineering methods that can be used to achieve custom domain patterns in LN crystals. In this section, we introduce how custom domain patterns in LN crystals can be used for applications in optics, acoustics, and LN patterning.

Optical

For optical applications, the most common use of domain patterns is to achieve quasi-phase matching (QPM) to compensate for phase-velocity mismatch of different waves. To achieve QPM, the spontaneous polarization of the LN crystal is inverted when the phase mismatch between the waves reaches 180°, resulting in a unidirectional energy flow over the propagation length when operating in the small signal conversion regime (see Fig. 20(e)). In the following, further information is provided

Table 2 | Comparison of domain inversion methods with available data.

Domain Inversion Method	Typical domain size	Poling of bulk LN	Poling of LNOI	Comment
Temperature mediated poling	> 4 μm[76] (period)	Yes	No	• Suitable for production of bulk PPLN with larger crystal thicknesses. • Control over period and duty cycle is comparatively less.
Defect diffusion	~21 μm[86] (period)	Yes	No	• Suitable for poling bulk LN. • May not be suitable for LNOI due to the high temperatures required.
Patterned surface electrodes poling	> 600 nm[96] (period)	Yes	Yes	• One of the most commonly used methods for domain engineering bulk LN and LNOI. • Excellent control over domain period. Less control over domain width or duty cycle. • High electrical voltage is required. • Wafer scale production is possible[146,147]. • Fur bulk LN *Z*-cut crystals are preferred, for LNOI *X* and *Z*-cut crystals are preferred.
Atomic force microscopy poling	> 50 nm[102]	Yes	Yes	• One of the highest resolution domain engineering methods. • Relatively high electrical voltage is required. • Domain engineering process is relatively slow as it is a serial process. • Potential issues of stitching for domain patterns larger than the writing field. • This method enables domain inversion in both *X* and *Z*-cut LNOI crystals.
Electron and ion beam poling	> 200 nm[124] (period)	Yes	Yes	• One of the highest resolution domain engineering methods. • Specialized equipment (e.g., SEM, EBL, FIB) required. • Domain engineering process is relatively slow as it is a serial process.
Light-assisted poling	> 5.25 μm[130] (period)	Yes	No	• An additional step involving electric field poling is necessary and utilized to invert domains in the *Z*-face of the LN crystal. • Has not yet been demonstrated in LNOI, although it may be possible.
Poling inhibition	> 3 μm[135] (period)	Yes	No	• An additional step involving electric field poling is necessary and utilized to write domains in the *Z*-face of the LN crystal. • May not be suitable for LNOI due to the high temperatures required. • Domain depth is generally low and depends on domain width[135].
Laser direct writing	> 100 nm[139]	Yes	No	• All optical poling and can be used to write domains in *Z*- face, *X* and *Y*-cut LN crystals. • Non-contact writing and precise domains can be achieved. • Domain depth is generally low and depends on domain width[139]. • May not be suitable for LNOI due to the high temperatures required.
Femtosecond laser writing	>30 nm[141]	Yes	No	• All optical poling that can be used to write and erase domain patterns in *X*, *Y*, and *Z*-cut LN crystals. • 3D domain patterns can be generated. • Non-contact writing and precise domains can be achieved. • Domains can have depths of tens of micron. • Translation to LNOI might be feasible.

for using domain engineered patterns for QPM for nonlinear optic, electro-optic, and polarization manipulation applications.

Nonlinear optic applications

While LN possesses both second order and third order nonlinear optical properties, it has traditionally been employed primarily for its second-order nonlinear optical characteristics. Notably, its nonlinear tensor features a dominant coefficient, d_{33} = 26 pm/V[94], aligned along the *Z*-axis. Second order nonlinear optical processes that LN crystals are used for, include second harmonic generation (SHG)[20,21,97], sum frequency generation (SFG)[148,149], difference frequency generation (DFG)[94] and spontaneous parametric down conversion (SPDC)[150]. In these nonlinear optical processes, custom domain patterns are crucial as they allow the QPM of light with different wavelengths / frequencies, which would naturally not be phase match due to the material dispersion of LN, particularly when modal phase matching[151] or birefringent phase matching[152,153] are not possible. In the following, the different nonlinear optical processes and their applications are briefly described.

In the SHG, photons with double the frequency of the input photons are produced, as illustrated in Fig. 20(a). SHG is used in applications such as the generation of light at wavelengths at which no efficient laser sources exist (e.g. frequency doubling of solid state lasers)[21] and the stabilization of optical frequency combs by frequency doubling the long wavelength tail of an octave spanning optical frequency comb and using the beat signal produced by the second harmonic wavelength and short wavelength tail of the octave spanning frequency comb for phase locking (f–$2f$ locking)[154].

In sum frequency generation (SFG) and difference frequency generation (DFG) (see Fig. 20(b, c)), light from two sources with different frequencies is used to generate a new frequency, which has either the sum or the difference of the two input frequencies. These processes find applications in diverse fields, including imaging[155], spectroscopy[156,157], sensing[12,158], parametric amplification[159] and optical communication applications[160].

Utilizing periodic domain engineering in LN allows for the efficient generation of entangled photon pairs via spontaneous parametric down-conversion (SPDC) as illustrated in Fig. 20(d). SPDC is a crucial element in quantum information processing and quantum communication applications[150,161], for example, by enabling the heralding of photons.

Further, the applications of domain-engineered lithium niobate (LN) extend beyond conventional uses to include nonlinear processes like high-harmonic generation and supercontinuum generation[12,163]. These processes benefit from the strong nonlinear coefficients of LN and the ability to engineer the phase-matching conditions, enabling efficient frequency conversion and the

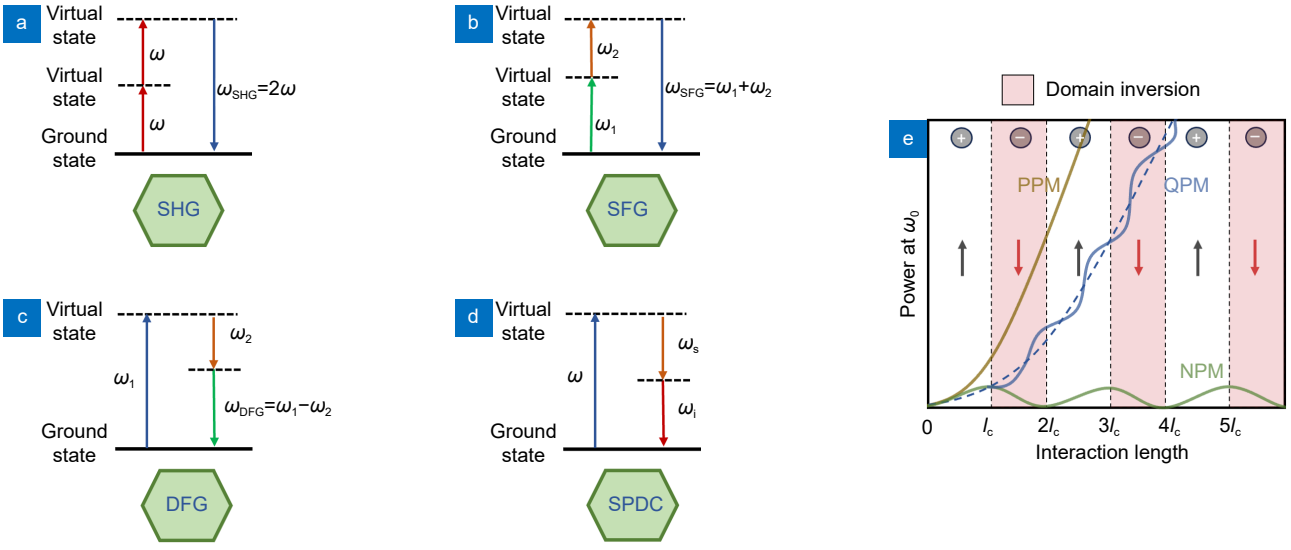

Fig. 20 | (**a**–**d**) Illustration of energy level diagram describing second harmonic generation (SHG), sum frequency generation (SFG), difference frequency generation (DFG), and spontaneous parametric down conversion (SPDC). (**e**) Illustration of the relative phase matching efficiencies for non-phase matching (NPM), quasi-phase matching (QPM) and perfect phase matching (PPM). The sign of the nonlinear susceptibility $\chi^{(2)}$ is inverted after each coherence length l_c for QPM. Figure redrawn from: (a–d) ref.[162], Elsevier; (e) ref.[28].

generation of new wavelengths. A broad spectrum of light from a narrow-band input, can be realized through the tailored nonlinear properties of domain-engineered LN[164]. The broad spectral output is particularly advantageous for applications in coherence tomography[165], spectroscopy, and high-capacity optical communications, as it allows for the generation of a wide range of wavelengths from a single source, enhancing the versatility and functionality of photonic devices.

In Table 3, an overview is given of experimental demonstration of second order nonlinear processes in bulk LN and LN waveguides, including the poling periods that are required for these processes. High-resolution domain engineering methods such as atomic force microscope poling and ion beam poling (Sections *Atomic force microscopy poling* and *Electron and ion beam poling*) are promising methods to achieve quasi-phase matching of counter-propagating optical waves, which require sub-micron domain patterns. This is very exciting for nonlinear optical processes in lithium niobate as such sub-micron domain periods can provide a pathway to integrated mirrorless optical parametric oscillator[166] on photonic integrated circuit chips.

Electro-optic applications

LN exhibits excellent electro-optical properties, which similar to the second order nonlinear properties manifest in the form of a tensor. The highest electro-optic tensor element is r_{33}, which has a value of 31 pm/V[25]. LN's electro-optic properties can be used to modulate light by applying an electrical signal, typically a microwave signal, to the LN crystal. The microwave signal modulates the refractive index of LN via the electro-optic effect $\Delta n_{\mathrm{e}} = -\left(n_{\mathrm{e}}^3 \gamma_{33} E\right)/2$, where n_{e} is the refractive index of the extraordinary wave and E is the applied electric field[177]. The modulation of the refractive index in turn modulates the phase of the optical wave traversing through the crystal. As the electro-optic effect in LN is relatively weak, interaction length in the order of several millimeters to a few centimeters is typically used to achieve sufficient modulation at moderate voltages.

If the optical wave and the microwave travel with different velocities (not being phase matched), then the two signals can go out of phase thereby reducing the modulation efficiency, which is more likely for high microwave frequencies and long electro-optic modulators. Similar to the case of the nonlinear optical applications, a custom domain pattern can be used to compensate for the velocity mismatch and achieve quasi-phase matching, as illustrated in Fig. 21. The poling period of the QPM structure is determined by $\Lambda = 1/\left(2f_{\mathrm{m}}\left(1/v_{\mathrm{m}} - 1/v_{\mathrm{o}}\right)\right)$, where v_{m} is the group velocity of the light wave, v_{o} is the phase velocity of the microwave and f_{m} is the modulation frequency[177,178]. It is important to note that unlike broadband electro-optic modulators that aim to achieve phase matching of the optical wave and the microwave, electro-optic modulators that uses a QPM structure have a narrower frequency operation window, which can be designed around a custom frequency[177–179].

Polarization manipulation

Periodic domain patterns in LN crystals can also be used to quasi-phase match TE and TM waveguide modes. Typically, these two modes would not couple as they are orthogonal. However, when an electric field is applied to the periodic domain pattern, the two orthogonal polarizations can couple via the electro-optical tensor element r_{51} in LN. One can consider the periodic domain inversion as a series of half-wave plates, which each rotate the polarization by an angle θ, which depends on the applied electric field strength E via $\theta = r_{51}E/\left[\left(1/n_{\mathrm{TE}}^2\right) - \left(1/n_{\mathrm{TM}}^2\right)\right]$. This shows that the coupling strength between TE and TM modes can be adjusted by the electric field strength. Furthermore, the process is wavelength selective as the $\Delta\lambda \approx 1.6\lambda_0/3N$ matching condition is only fulfilled in a certain wavelength range[181], where N is the number of inverted domains. These properties can be used to rotate the polarization of a selected wavelength range in LN, which enables the demonstration of Solc-type wavelength filters in LN bulk crystals[181,182] and waveguides[183] by using external polarizers.

Acoustic

Integrating bulk and surface acoustic waves (BAW and SAW) into microdevices encompasses a wide range of applications in fields such as optical communication[184], electronics[185], biosensors[185–187] , and gyroscopics[188]. LN is a highly attractive material for acoustic applications thanks to its piezoelectric properties and relatively high electro-mechanic coupling coefficient, which allows the efficient excitation and detection of acoustic waves, e.g., with inter digital transducer (IDT) (see Fig. 22(a)). The ability to create custom domain patterns in LN is desirable for acoustic applications as it provides an additional degree of freedom in the design of acoustic devices, en-

Table 3 | Overview of different lithium niobate nonlinear optical device designs.

References	Type		Method of poling	Length (mm)	Poling period (μm)	Normalized efficiency (%/W/cm²)	Overall efficiency (%/W)	Conversion efficiency (%)	Pump power (mW)	Nonlinear process
ref.[20]	Thin film	Thin film LNOI *X*-cut (600 nm)	Electric field poling (EFP)	21	4.30–4.37 (Adapted poling)	2150	9500	82.5	20.3	Second harmonic generation (SHG)
ref.[21]		Thin film LNOI *X*-cut (600 nm)	Electric field poling (EFP)	4	4.1	2600	416	53	220	Second harmonic generation (SHG)
ref.[167]		SiN-TFLN *X*-cut(300 nm)	Electric field poling (EFP)	4.8	4.98	1160	267	Not available	Not available	Second harmonic generation (SHG)
ref.[150]		SiN-TFLN *X*-cut(300 nm)	Electric field poling (EFP)	4.8	4.87	230 (SHG)	53 (SHG)	Not available	Not available	Photon pair generation (SPDC)
ref.[161]		Thin film LNOI *X*-cut (300 nm)	Electric field poling (EFP)	5	2.8	1700 (SHG)	425 (SHG)	Not available	Not available	Photon pair generation (SPDC)
ref.[168]		Thin film LNOI *X*-cut (600 nm)	Electric field poling (EFP)	10	3.66	2618	2618 (SFG)	24.17	10.96 (~1317nm), 22.38 (1064nm)	Sum frequency generation (SFG)
ref.[169]	Bulk	Direct-Bonded PPZnLN	Electric field poling (EFP)	50	17	96	2400	92	160	Second harmonic generation (SHG)
ref.[170]		Proton exchange	Electric field poling (EFP)	60	14.74	38	1400	99	900	Second harmonic generation (SHG)
ref.[171]		MgO:PPLN	Electric field poling (EFP)	20	17.3	62	248	58	7000	Second harmonic generation (SHG)
ref.[172]		Zinc-indiffused MgO:PPLN	Not specified	40	18.3	6.29	100.6	70	1590	Second harmonic generation (SHG)
ref.[173]		MgO:PPLN *Z*-cut	Electric field poling (EFP)	50	10.2	1.32	33 (SFG)	Not available	Not available	Sum frequency generation (SFG)
ref.[174]		MgO:PPLN *Z*-cut	Electric field poling (EFP)	40	10.1–10.4	4.06	65 (SFG)	Not available	Not available	Sum frequency generation (SFG)
ref.[175]		MgO: PPLN crystal	Not specified	50	32.16	0.0228	0.57 (DFG)	Not available	Not available	Difference frequency generation (DFG)
ref.[176]		PPLN Crystal *Z*-cut	Electric field poling (EFP)	17.5	22.0	0.0068	0.021 (DFG)	Not available	Not available	Difference frequency generation (DFG)

abling, for example, the generation of acoustic waves with coplanar electrodes and monolithically uniform phononic crystals, which will be discussed in more detail below.

Surface acoustic wave generation

For most of the acoustic applications, control over the excitation and propagation of acoustic waves is crucial for device performance. However, for acoustic devices that are required to operate at GHz frequencies, it can be challenging to achieve this with IDTs, as the excitation frequency f of the SAW depends on the IDT period Λ_{IDT} by $f = v_{\mathrm{p}}/\Lambda_{\mathrm{IDT}}$, where v_{p} is the SAW phase velocity of the LN crystal. From the equation, one can see that IDTs that operate at GHz frequencies require a micron or sub-micron IDT period, when assuming a SAW phase velocity of ~3488 m/s (*Y*-cut, *Z*-propagating). This presents challenges two-fold: (i) the fabrication of sub-micron

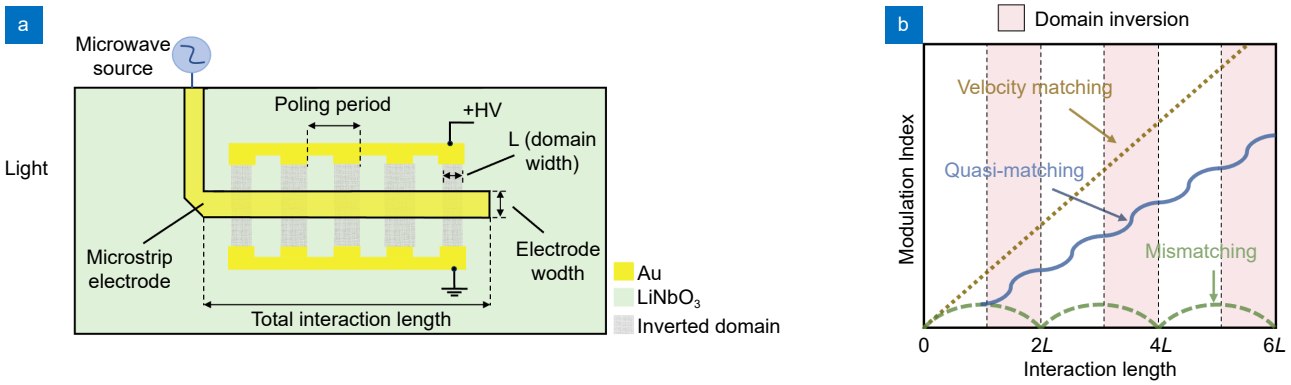

Fig. 21 | (**a**) Illustration of the EO modulator with open-circuited-end microstrip electrode and inversion sections. (**b**) The modulation index as a function of interaction length in the case of velocity matching, quasi-matching and mismatching. Figure redrawn from: (a) ref.[180], (b) ref.[178], IEEE.

fingers, which have a width of $\Lambda_{IDT}/4$, over a large area is difficult as there is a chance for short-circuiting and damage due to the small gap between electrode fingers[189] and (ii) if high electrical powers are used for the excitation of acoustic waves, the conductivity for narrow finger widths can cause thermal issues and malfunction of the IDT[189].

A way to overcome these challenges is the use of custom domain patterns in LN crystal, which are also known as piezoelectric acoustic superlattice (ASL)[190]. An ASL is a PPLN structure, which has a change in piezoelectric constant sign every period, thanks to the domain pattern. In such an ASL structure, wide coplanar electrodes are placed normal to the domain pattern with a gap in between the electrodes (see Fig. 22(b)). If an electrical signal is applied to the electrodes the period inverted domain pattern creates a periodic surface displacement with a period determined by the poling pattern. The operation frequency of the acoustic transducer is therefore determined by the poling period of the domain pattern $f = v_p/\Lambda_{ASL}$, where a domain width is $\Lambda_{ASL}/2$. An ASL SAW transducer, therefore, relaxes the fabrication challenges that may cause short circuiting due to the larger electrode dimensions. Furthermore, higher electrical powers can be applied to electrodes thanks to the increased conductivity of the coplanar electrodes. This makes ASL an attractive candidate for SAW generation and detection, which has enabled acoustic devices such as an electrical driven polarization rotator[16], as shown in Fig. 22(c).

One should note that ASL transducers are typically fabricated on *Z*-cut LN crystal, due to the availability of mature domain engineering methods of electric field poling. However, domain engineering methods such as atomic force microscopy poling or ion beam poling provide avenues to achieve excellent quality sub-micron domain patterns, which provides a pathway to acoustic devices that can operate at tens of GHz. Furthermore, for certain applications where high SAW energies are required, such as in microfluidic actuation[191], the substrate of choice is 128° *YX*-cut LN. Poling of such crystal can be done by domain engineering methods such as the direct writing of domains with lasers[16,192].

Phononic bandgaps

Surface phononic bandgap structures are important for controlling the propagation of phonons in a medium. These structures have intensive application in fields such as biosensing[186,191], quantum physics[195,196], and microfluidics[191]. A point to be noted is that, for example, for quantum physics applications, the interaction of random phonons from the environment is not desired. To avoid such phonon interactions, phonon cavities are created where phonons with a particular frequency are trapped. Reports have shown that phononic bandgap structures can be formed by an array of pillars or holes[197], but both need many steps of machining and can provide integration challenges. These limitations can be overcome when a mechanically and dielectrically homogeneous material is used to create phononic bandgap, which is possible by domain inversion of piezoelectric crystals such as LN[198], as discussed in the previous section. A bandgap is created by phonon-polariton coupling and the phonon frequency can be chosen by the period of the domains. This has enabled the demonstration of 2D phononic crystals in *Z*-cut LN using a 2D hexagonal poling pattern[15], as can be seen in Fig. 23(c) and 23(d). Furthermore, placing a defect in the phononic

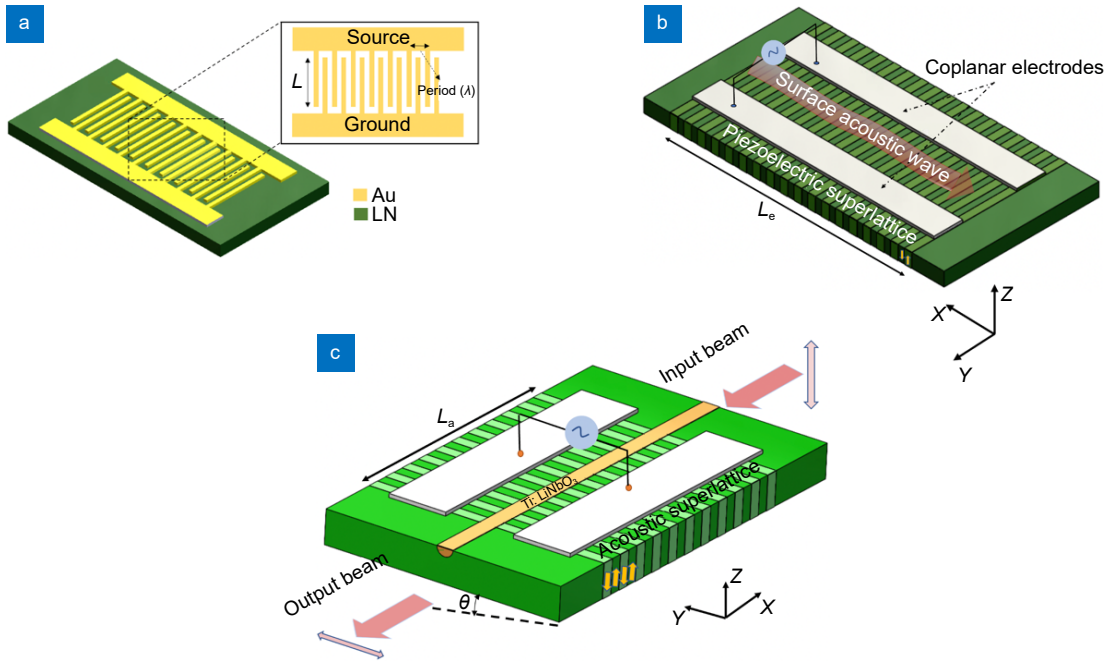

Fig. 22 | (**a**) Schematic of an IDT on a LN substrate. (**b**) Basic structure of ASL based-on *ZX*-cut PPLN with coplanar electrodes. (**c**) Schematic of the integrated AO polarization converter based on ASL on *Z*-cut PPLN with coplanar uniform electrodes. Figure redrawn from: (a) ref.[193], (b) ref.[194], AIP Publishing; (c) ref.[16], Optical Society of America.

crystal provides a means to engineer the bandgap to form a phonon cavity. This has been demonstrated in a 1D photonic crystal by placing a single domain defect in the center of the poled structure[199] as illustrated in Fig. 23(a) and 23(b).

Surface patterning

The patterning of LN crystals enables the fabrication of LN devices such as single crystal cantilevers, alignment grooves for fibers, micro lens, and photonic and phononic waveguides and resonator devices. However, the controlled patterning of LN can be challenging due to the inertness of LN. Although significant progress has been made in recent years by focused ion beam (FIB) and reactive ion etching (RIE), they face limitations on the area that can be patterned, the aspect ratio of the fabrication and the sidewalls (for example, argon ion milling). Differential etching of LN can be useful as an additional surface patterning method for LN. Differential etching of LN allows the micro-structuring of LN since each crystal face of LN exhibits different etch rates when being etched by hydrofluoric acid (HF). For example, the etch rate of the $-Z$ face is about 1μm/h, whereas the $+Z$ face is not affected by HF[40]. Likewise, the $+Y$ (~0.04–0.05 μm/h) and $-Y$ (~0.08–0.11 μm/h) faces also have different etch rates, but the difference between the etch rates is less[42]. This means that domain patterns can be translated into a surface topography, forming microstructures in LN. This has proven to be an efficient method to form microstructures in LN[200], as shown in Fig. 24(a) and has been used for the fabrication of a 2D phononic crystal operating at GHz frequencies (Fig. 24(b))[201] by using a high-resolution domain patterning method[139]. Recently, a fork grating for generating vortex beams has been fabricated through domain patterning and chemical etching in *X*-cut LN[143].

The microstructures formed by differential etching can have sharp tips or edges, as shown in Fig. 24(c), which is not desirable for certain applications. Surface tension reshaping[202] can be used to form smooth microstructures, which can be achieved by thermal annealing the LN samples below curie temperature (e.g., 1130 °C for 50 minutes) with continuing oxygen flow to avoid lithium out diffusion. By this annealing process reshaping occurs, which in Fig. 24(d) was used to form an array of smooth micro lens[202]. This makes surface patterning by differential etching of domains a promising technique to form smooth microstructures in LN.

Outlook

The future of LNOI domain engineering is poised for exciting breakthroughs in integrated photonics and

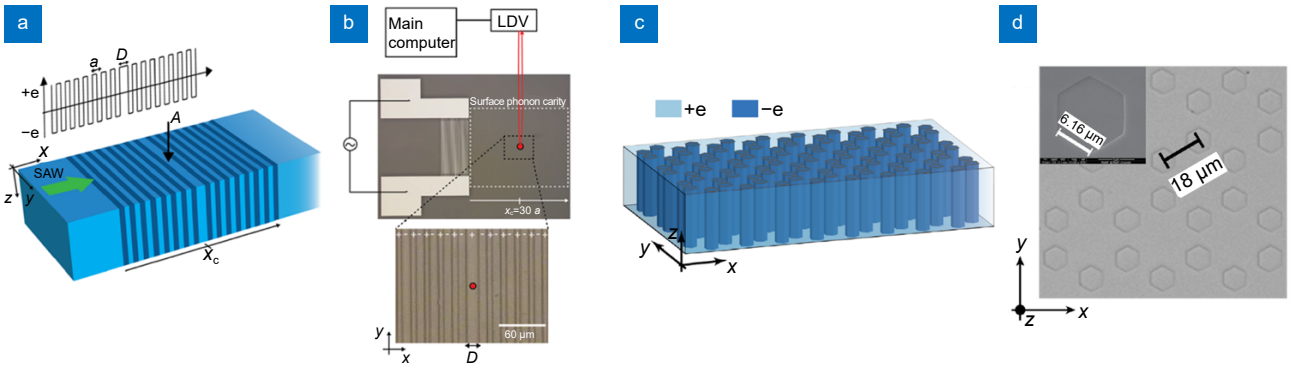

Fig. 23 | (**a**) Illustration of a surface phonon cavity with a bandgap structure consisting of regular poling with period a, and with an included defect of width *D*. (**b**) Microscope image of the fabricated surface phonon cavity and the IDTs used to generate the SAW. The poled bandgap region is indicated by the larger white dashed rectangle and the region with the defect is indicated by the smaller dark dashed rectangle. (**c**) Schematic of the surface phonon-polariton phononic crystal formed from domain-inverted hexagonal inclusions. (**d**) An optical micrograph of the back side of the substrate after HF etching, with a scanning electron microscope image inset showing the hexagonal domain-inverted inclusion. Figure reproduced with permission from: (a, b) ref.[199], WILEY-VCH Verlag GmbH & Co. KGaA, Weinheim; (c, d) ref.[15], American Physical Society.

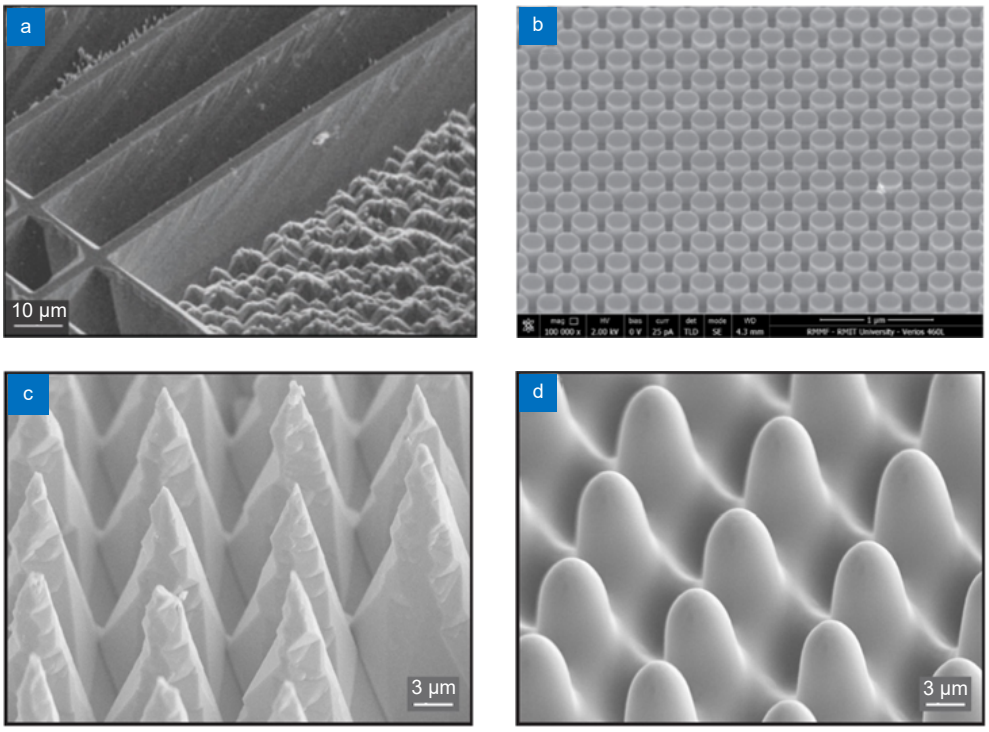

Fig. 24 | (**a**) SEM image (tilted at 45°) of large aspect ratio surface structures in LN produced by extended etching of a domain pattern for tens of hours. The long sections of the slabs are aligned along the *y*-axis of the crystal thus producing *X*-face sidewall surfaces which etch much slower than −*Z* face. (**b**) SEM 45˚ angle view image of a fabricated nanopillar phononic crystals in LN. (**c**) SEM images of the micro-structured LN crystal surface (45° tilted) after deep etching of a 2D lattice of inverted ferroelectric domains. (**d**) shows the micro-structured LN crystal after thermal treatment. Figure reproduced with permission from: (a) ref.[125], John Wiley and Sons; (b) ref. [201], American Physical Society; (c, d) ref.[202], Optical Society of America.

acoustics. The required period size for these applications is primarily dictated by the target frequency, spanning from a few microns to sub-microns. EFP, the most commonly used method, is favored for its maturity and feasibility[20]. However, maintaining domain uniformity and control over individual domain dimensions remains a challenge. EFP is predominantly demonstrated in *X*-cut LNOI due to the ease of coplanar electrode placement. In *Z*-cut LNOI, a conductive bottom electrode is still necessary. This bottom electrode can either be in direct

contact with the LN layer (which is less attractive for certain optical applications) or beneath an insulating SiO_2 layer to promote domain growth (suitable for optical applications). Demonstrations involving poling at elevated temperatures have shown that it facilitates axial domain growth close to the LN-silica interface in *Z*-cut LNOI. However, further advancements are required in both *X*-cut and *Z*-cut LNOI to make these processes more flexible and robust.

Creating fine sub-micron periods with EFP is a formidable task, primarily due to the risk of lateral domain merging from closely spaced finger electrodes. Applying high-voltage pulses to such narrow electrodes can lead to their premature domain spread and potential merging before complete inversion in depth[96]. Alternative methods for creating fine submicron domains in LNOI, such as AFM and ion-beam poling, have shown promise. AFM is a more mature technique for *Z*-cut LNOI, with demonstrated domain sizes down to 50 nm[102]. However, domain stability remains a crucial aspect. AFM for *Z*-cut poling faces challenges similar to EFP, potentially impacting optical application efficiency due to bottom electrodes. Techniques like operating at higher temperatures during poling are also used in AFM[47]. A significant advancement in AFM-based domain inversion is the achievement of domain inversion in *X*-cut LNOI. Although still in its early stages, this technique shows promise and further investigation into domain stability is necessary[106]. These advancements suggest that AFM could become a significant method for poling submicron domains in both *X* and *Z*-cut LNOI. AFM also offers the advantage of individual domain control, which is not possible with EFP. Ion-beam poling is another strong contender for sub-micron domain poling, especially for *Y* and *Z*-cut crystals. Demonstrations in *Z*-cut LNOI have been successful, and ongoing advancements are promising[124].

A highly potential yet unexplored method for poling LNOI is all-optical poling. The main limitation has been the absorption of light by the Si substrate and the aftereffects, such as the delamination of layers in LNOI due to the high temperatures generated during the process. However, LNOI with LN or sapphire as the substrate could utilize this technique. In bulk LN, optical poling techniques have proven effective for writing and erasing sub-micron domains. Adapting this to LNOI could enable domain engineering of any crystal cut of LNOI. In the case of LNOI with a Si substrate, modifying the laser focusing and other optics could facilitate domain poling. In conclusion, EFP and AFM are excellent for poling *X* and *Z*-cut LNOI. However, further exploration and advancements in optical poling techniques could open new opportunities for precise domain engineering in any cut of LNOI.

Summary

In this review article, we have surveyed an array of methods for engineering the ferroelectric domains of LN crystals that have been reported over the past decades. The domain engineering methods reviewed include temperature-mediated poling, defect diffusion, electric field poling, and light-assisted and all-optical poling. These domain engineering methods are constantly being improved, with a focus on exploring domain engineering methods that provide high-resolution domain patterning with excellent reproducibility. Furthermore, the translation of the domain engineering methods to the thin-film LNOI platform is attracting a lot of attention, as the thin-film LNOI platform is highly attractive for the next generation of acoustic and photonic integrated circuit devices. Indeed, LN is a highly attractive material for generating and manipulating acoustic and electromagnetic waves over a spectral range that covers nearly 4 orders of magnitude for acoustics and nearly five orders of magnitude for electromagnetics[12]. The ability to fabricate exquisite domain patterns in LN ensures that the diverse applications that LN is used for are ever-growing.

References

1. Zachariasen FWH. Standard x-ray diffraction powder patterns. [Kl.] 1 Mat. *Mat Naturv-Idensk Kl* **4**, 1–8 (1928).
2. Ballman AA. Growth of piezoelectric and ferroelectric materials by the czochraiski technique. *J Am Ceram Soc* **48**, 112–113 (1965).
3. Nassau K, Levinstein HJ, Loiacono GM. Ferroelectric lithium niobate. 2. Preparation of single domain crystals. *J Phys Chem Solids* **27**, 989–996 (1966).
4. Popescu ST, Petris A, Vlad IV. Interferometric measurement of the pyroelectric coefficient in lithium niobate. *J Appl Phys* **113**, 043101 (2013).
5. Smith RT, Welsh FS. Temperature dependence of the elastic, piezoelectric, and dielectric constants of lithium tantalate and lithium niobate. *J Appl Phys* **42**, 2219–2230 (1971).
6. Peterson GE, Ballman AA, Lenzo PV et al. Electro-optic properties of $LiNbO_3$. *Appl Phys Lett* **5**, 62–64 (1964).
7. Ashkin A, Boyd GD, Dziedzic JM et al. Optically-induced refractive index inhomogeneities in $LiNbO_3$ AND $LiTaO_3$. *Appl Phys Lett* **9**, 72–74 (1966).
8. Bell DT, Li RCM. Surface-acoustic-wave resonators. *Proc IEEE* **64**, 711–721 (1976).

9. Graham RA. Pressure dependence of the piezoelectric polarization of $LiNbO_3$ and $LiTaO_3$. *Ferroelectrics* **10**, 65–69 (1976).
10. Smith RG, Nassau K, Galvin MF. Efficient continuous optical second-harmonic generation. *Appl Phys Lett* **7**, 256–258 (1965).
11. Rauber A. In Kaldis E. *Current Topics in Materials Science, Vol. 1*, (North-Holland, Amsterdam, 1978).
12. Boes A, Chang L, Langrock C et al. Lithium niobate photonics: unlocking the electromagnetic spectrum. *Science* **379**, eabj4396 (2023).
13. Ruppel CCW, Reindl L, Weigel R. SAW devices and their wireless communications applications. *IEEE Microw Mag* **3**, 65–71 (2002).
14. Wooten EL, Kissa KM, Yi-Yan A et al. A review of lithium niobate modulators for fiber-optic communications systems. *IEEE J Sel Top Quantum Electron* **6**, 69–82 (2000).
15. Yudistira D, Boes A, Djafari-Rouhani B et al. Monolithic phononic crystals with a surface acoustic band gap from surface phonon-polariton coupling. *Phys Rev Lett* **113**, 215503 (2014).
16. Yudistira D, Janner D, Benchabane S et al. Integrated acousto-optic polarization converter in a *ZX*-cut $LiNbO_3$ waveguide superlattice. *Opt Lett* **34**, 3205–3207 (2009).
17. Yamada M, Nada N, Saitoh M et al. First-order quasi-phase matched $LiNbO_3$ waveguide periodically poled by applying an external field for efficient blue second-harmonic generation. *Appl Phys Lett* **62**, 435–436 (1993).
18. Wu RB, Wang M, Xu J et al. Long low-loss-litium niobate on insulator waveguides with sub-nanometer surface roughness. *Nanomaterials* **8**, 910 (2018).
19. Desiatov B, Shams-Ansari A, Zhang M et al. Ultra-low-loss integrated visible photonics using thin-film lithium niobate. *Optica* **6**, 380–384 (2019).
20. Chen PK, Briggs I, Cui CH et al. Adapted poling to break the nonlinear efficiency limit in nanophotonic lithium niobate waveguides. *Nat Nanotechnol* **19**, 44–50 (2024).
21. Wang C, Langrock C, Marandi A et al. Ultrahigh-efficiency wavelength conversion in nanophotonic periodically poled lithium niobate waveguides. *Optica* **5**, 1438–1441 (2018).
22. Lu JJ, Surya JB, Liu XW et al. Periodically poled thin-film lithium niobate microring resonators with a second-harmonic generation efficiency of 250, 000%/W. *Optica* **6**, 1455–1460 (2019).
23. He MB, Xu MY, Ren YX et al. High-performance hybrid silicon and lithium niobate Mach–Zehnder modulators for 100 Gbit s^{-1} and beyond. *Nat Photonics* **13**, 359–364 (2019).
24. Wang C, Zhang M, Chen X et al. Integrated lithium niobate electro-optic modulators operating at CMOS-compatible voltages. *Nature* **562**, 101–104 (2018).
25. Zhang M, Wang C, Kharel P et al. Integrated lithium niobate electro-optic modulators: when performance meets scalability. *Optica* **8**, 652–667 (2021).
26. Weis RS, Gaylord TK. Lithium niobate: summary of physical properties and crystal structure. *Appl Phys A* **37**, 191–203 (1985).
27. Boes AS. Laser light induced domain engineering of lithium niobate for photonic and phononic applications (RMIT University, Melbourne, 2016).
28. Ying Y. Light-assisted domain engineering, waveguide fabrication and microstructuring of lithium niobate (University of Southampton, Southampton, 2010).
29. Abrahams SC, Reddy JM, Bernstein JL. Ferroelectric Lithium niobate. 3. Single crystal X-ray diffraction study at 24°C. *J Phys Chem Solids* **27**, 997–1012 (1966).
30. Abrahams SC, Hamilton WC, Reddy JM. Ferroelectric lithium niobate. 4. Single crystal neutron diffraction study at 24°C. *J Phys Chem Solids* **27**, 1013–1018 (1966).
31. Wong KK. *Properties of Lithium Niobate* (INSPEC/Institution of Electrical Engineers, London, 2002).
32. Gopalan V, Sanford NA, Aust JA et al. Crystal growth, characterization, and domain studies in lithium niobate and lithium tantalate ferroelectrics. *Handb Adv Electron Photonic Mater Dev* **4**, 57–114 (2001).
33. Gopalan V, Dierolf V, Scrymgeour DA. Defect-domain wall interactions in trigonal ferroelectrics. *Annu Rev Mater Res* **37**, 449–489 (2007).
34. Prokhorov AM, Kuz'minov YS. *Physics and Chemistry of Crystalline Lithium Niobate* (Hilger, Bristol, 1990).
35. Schirmer FO, Thiemann O, Wöhlecke M. Defects in $LiNbO_3$-I. Experimental aspects. *J Phys Chem Solids* **52**, 185–200 (1991).
36. Lines ME, Glass AM. *Principles and Applications of Ferroelectrics and Related Materials* (Oxford University Press, Oxford, 2001).
37. Gui L, Hu H, Garcia-Granda M et al. Local periodic poling of ridges and ridge waveguides on X- and Y-Cut $LiNbO_3$ and its application for second harmonic generation. *Opt Express* **17**, 3923–3928 (2009).
38. Jungk T, Hoffmann Á, Soergel E. New insights into ferroelectric domain imaging with piezoresponse force microscopy. In Ferraro P, Grilli S, De Natale P. *Ferroelectric Crystals for Photonic Applications: Including Nanoscale Fabrication and Characterization Techniques* 205–226 (Springer, Berlin, 2014).
39. Nassau K, Levinstein HJ, Loiacono GM. Ferroelectric lithium niobate. 1. Growth, domain structure, dislocations and etching. *J Phys Chem Solids* **27**, 983–988 (1966).
40. Sones CL, Mailis S, Brocklesby WS et al. Differential etch rates in z-cut $LiNbO_3$ for variable HF/HNO_3 concentrations. *J Mater Chem* **12**, 295–298 (2002).
41. Niizeki N, Yamada T, Toyoda H. Growth ridges, etched hillocks, and crystal structure of lithium niobate. *Jpn J Appl Phys* **6**, 318–327 (1967).
42. Valdivia CE. Light-induced ferroelectric domain engineering in lithium niobate & lithium tantalate (University of Southampton, Southampton, 2007).
43. Bermúdez V, Caccavale F, Sada C et al. Etching effect on periodic domain structures of lithium niobate crystals. *J Cryst Growth* **191**, 589–593 (1998).
44. Güthner P, Dransfeld K. Local poling of ferroelectric polymers by scanning force microscopy. *Appl Phys Lett* **61**, 1137–1139 (1992).
45. Soergel E. Piezoresponse force microscopy (PFM). *J Phys D Appl Phys* **44**, 464003 (2011).
46. Soergel E. Visualization of ferroelectric domains in bulk single crystals. *Appl Phys B* **81**, 729–751 (2005).
47. Slautin BN, Zhu H, Shur VY. Submicron periodical poling by local switching in ion sliced lithium niobate thin films with a dielectric layer. *Ceram Int* **47**, 32900–32904 (2021).
48. Qian YZ, Zhang ZQ, Liu YZ et al. Graphical direct writing of macroscale domain structures with nanoscale spatial resolu-

tion in nonpolar-cut lithium niobate on insulators. *Phys Rev Appl* **17**, 054049 (2022).
49. Reitzig S, Rüsing M, Zhao J et al. "Seeing is believing"—in-depth analysis by co-imaging of periodically-poled x-cut lithium niobate thin films. *Crystals* **11**, 288 (2021).
50. Jungk T, Hoffmann Á, Soergel E. Contrast mechanisms for the detection of ferroelectric domains with scanning force microscopy. *New J Phys* **11**, 033029 (2009).
51. Rüsing M, Zhao J, Mookherjea S. Second harmonic microscopy of poled x-cut thin film lithium niobate: Understanding the contrast mechanism. *J Appl Phys* **126**, 114105 (2019).
52. Berth G, Quiring V, Sohler W et al. Depth-resolved analysis of ferroelectric domain structures in Ti: PPLN waveguides by nonlinear confocal laser scanning microscopy. *Ferroelectrics* **352**, 78–85 (2007).
53. Huang XY, Wei DZ, Wang YM et al. Second-harmonic interference imaging of ferroelectric domains through a scanning microscope. *J Phys D Appl Phys* **50**, 485105 (2017).
54. Kaneshiro J, Uesu Y, Fukui T. Visibility of inverted domain structures using the second harmonic generation microscope: comparison of interference and non-interference cases. *J Opt Soc Am B* **27**, 888–894 (2010).
55. Wei DZ, Liu DM, Hu XP et al. Superposed second-harmonic Talbot self-image from a PPLT crystal. *Laser Phys Lett* **11**, 095402 (2014).
56. Zhao J, Rüsing M, Mookherjea S. Optical diagnostic methods for monitoring the poling of thin-film lithium niobate waveguides. *Opt Express* **27**, 12025–12038 (2019).
57. Mackwitz P, Rüsing M, Berth G et al. Periodic domain inversion in x-cut single-crystal lithium niobate thin film. *Appl Phys Lett* **108**, 152902 (2016).
58. Zhang B, Wang L, Chen F. Recent advances in femtosecond laser processing of $LiNbO_3$ crystals for photonic applications. *Laser Photonics Rev* **14**, 1900407 (2020).
59. Chen X, Karpinski P, Shvedov V et al. Ferroelectric domain engineering by focused infrared femtosecond pulses. *Appl Phys Lett* **107**, 141102 (2015).
60. Sheng Y, Best A, Butt HJ et al. Three-dimensional ferroelectric domain visualization by Čerenkov-type second harmonic generation. *Opt Express* **18**, 16539–16545 (2010).
61. Deng XW, Chen XF. Domain wall characterization in ferroelectrics by using localized nonlinearities. *Opt Express* **18**, 15597–15602 (2010).
62. Roppo V, Kalinowski K, Sheng Y et al. Unified approach to Čerenkov second harmonic generation. *Opt Express* **21**, 25715–25726 (2013).
63. Chen X, Karpinski P, Shvedov V et al. Quasi-phase matching via femtosecond laser-induced domain inversion in lithium niobate waveguides. *Opt Lett* **41**, 2410–2413 (2016).
64. Gopalan V, Mitchell TE. *In situ* video observation of 180° domain switching in $LiTaO_3$ by electro-optic imaging microscopy. *J Appl Phys* **85**, 2304–2311 (1999).
65. Müller M, Soergel E, Buse K. Visualization of ferroelectric domains with coherent light. *Opt Lett* **28**, 2515–2517 (2003).
66. Gopalan V, Gupta MC. Origin of internal field and visualization of 180° domains in congruent $LiTaO_3$ crystals. *J Appl Phys* **80**, 6099–6106 (1996).
67. Younesi M, Geiss R, Rajaee S et al. Periodic poling with a micrometer-range period in thin-film lithium niobate on insulator. *J Opt Soc Am B* **38**, 685–691 (2021).
68. Armstrong JA, Bloembergen N, Ducuing J et al. Interactions between light waves in a nonlinear dielectric. *Phys Rev* **127**, 1918–1939 (1962).
69. Fedulov A, Shapiro ZI, Ladyzhinskii PB. The growth of crystals of $LiNbO_3$, $LiTaO_3$ and $NaNbO_3$ by the Czochralski method. *Sov Phys Crystallogr* **10**, 218–220 (1965).
70. Nassau K, Levinstein HJ. Ferroelectric behavior of lithium niobate. *Appl Phys Lett* **7**, 69–70 (1965).
71. Nakamura K, Ando H, Shimizu H. Ferroelectric domain inversion caused in $LiNbO_3$ plates by heat treatment. *Appl Phys Lett* **50**, 1413–1414 (1987).
72. Miyazawa S. Ferroelectric domain inversion in Ti-diffused $LiNbO_3$ optical waveguide. *J Appl Phys* **50**, 4599–4603 (1979).
73. Bermúdez V, Callejo D, Vilaplana R et al. Engineering of lithium niobate domain structure through the off-centered Czochralski growth technique. *J Cryst Growth* **237**–239, 677–681 (2002).
74. Lim EJ, Fejer MM, Byer RL. Second-harmonic generation of green light in periodically poled planar lithium niobate waveguide. *Electron Lett* **25**, 174–175 (1989).
75. Feisst A, Koidl P. Current induced periodic ferroelectric domain structures in $LiNbO_3$ applied for efficient nonlinear optical frequency mixing. *Appl Phys Lett* **47**, 1125–1127 (1985).
76. Naumova II, Evlanova NF, Gliko OA et al. Czochralski-grown lithium niobate with regular domain structure. *Ferroelectrics* **190**, 107–112 (1997).
77. Sada C, Argiolas N, Bazzan M. On the dynamics of periodically-poled lithium niobate formation by off-center Czochralski technique. *Appl Phys Lett* **79**, 2163–2165 (2001).
78. Ming NB, Hong JF, Feng D. The growth striations and ferroelectric domain structures in Czochralski-grown $LiNbO_3$ single crystals. *J Mater Sci* **17**, 1663–1670 (1982).
79. Feng D, Ming NB, Hong JF et al. Enhancement of second-harmonic generation in $LiNbO_3$ crystals with periodic laminar ferroelectric domains. *Appl Phys Lett* **37**, 607–609 (1980).
80. Poberaj G, Koechlin M, Sulser F et al. Ion-sliced lithium niobate thin films for active photonic devices. *Opt Mater* **31**, 1054–1058 (2009).
81. Nakamura K, Shimizu H. Local domain inversion in ferroelectric crystals and its application to piezoelectric devices. In *Proceedings of IEEE Ultrasonics Symposium* 309–318 (IEEE, 1989); http://doi.org/10.1109/ULTSYM.1989.67000.
82. Rosenman G, Kugel VD, Angert N. Domain inversion in $LiNbO_3$ optical waveguides. *Ferroelectrics* **157**, 111–116 (1994).
83. Kugel VD, Rosenman G. Polarization reversal in $LiNbO_3$ crystals under asymmetric diffusion conditions. *Appl Phys Lett* **65**, 2398–2400 (1994).
84. Thaniyavarn S, Findakly T, Booher D et al. Domain inversion effects in Ti-$LiNbO_3$ integrated optical devices. *Proc SPIE* **559**, 124–128 (1985).
85. Rosenman G, Kugel VD, Shur D. Diffusion-induced domain inversion in ferroelectrics. *Ferroelectrics* **172**, 7–18 (1995).
86. Huang CY, Lin CH, Chen YH et al. Electro-optic Ti: PPLN waveguide as efficient optical wavelength filter and polarization mode converter. *Opt Express* **15**, 2548–2554 (2007).
87. Webjörn J, Pruneri V, Russell PSJ et al. Quasi-phase-matched blue light generation in bulk lithium niobate, electrically poled via periodic liquid electrodes. *Electron Lett* **30**, 894–895 (1994).
88. Liang LY, Wang FL, Sang YH et al. Facile approach for the pe-

riodic poling of MgO-doped lithium niobate with liquid electrodes. *CrystEngComm* **21**, 941–947 (2019).
89. Miller GD. Periodically poled lithium niobate: modeling, fabrication, and nonlinear optical performance (Stanford University , Stanford, 1998).
90. Stivala S, Pasquazi A, Colace L et al. Guided-wave frequency doubling in surface periodically poled lithium niobate: competing effects. *J Opt Soc Am B* **24**, 1564–1570 (2007).
91. Mizuuchi K, Morikawa A, Sugita T et al. Electric-field poling in Mg-doped $LiNbO_3$. *J Appl Phys* **96**, 6585–6590 (2004).
92. Chang L, Li YF, Volet N et al. Thin film wavelength converters for photonic integrated circuits. *Optica* **3**, 531–535 (2016).
93. Nagy JT, Reano RM. Reducing leakage current during periodic poling of ion-sliced x-cut MgO doped lithium niobate thin films. *Opt Mater Express* **9**, 3146–3155 (2019).
94. Chang L, Boes A, Shu HW et al. Second order nonlinear photonic integrated platforms for optical signal processing. *IEEE J Sel Top Quantum Electron* **27**, 5100111 (2021).
95. Chen JY, Tang C, Ma ZH et al. Efficient and highly tunable second-harmonic generation in Z-cut periodically poled lithium niobate nanowaveguides. *Opt Lett* **45**, 3789–3792 (2020).
96. Zhao J, Rüsing M, Roeper M et al. Poling thin-film x-cut lithium niobate for quasi-phase matching with sub-micrometer periodicity. *J Appl Phys* **127**, 193104 (2020).
97. Boes A, Chang L, Nguyen T et al. Efficient second harmonic generation in lithium niobate on insulator waveguides and its pitfalls. *J Phys Photonics* **3**, 012008 (2021).
98. Rosenman G, Urenski P, Agronin A et al. Submicron ferroelectric domain structures tailored by high-voltage scanning probe microscopy. *Appl Phys Lett* **82**, 103–105 (2003).
99. Agronin A, Rosenwaks Y, Rosenman G. Ferroelectric domain reversal in $LiNbO_3$ crystals using high-voltage atomic force microscopy. *Appl Phys Lett* **85**, 452–454 (2004).
100. Lilienblum M, Ofan A, Hoffmann Á et al. Low-voltage nanodomain writing in He-implanted lithium niobate crystals. *Appl Phys Lett* **96**, 082902 (2010).
101. Ofan A, Lilienblum M, Gaathon O et al. Large-area regular nanodomain patterning in He-irradiated lithium niobate crystals. *Nanotechnology* **22**, 285309 (2011).
102. Ma JN, Cheng XY, Zheng NC et al. Fabrication of 100-nm-period domain structure in lithium niobate on insulator. *Opt Express* **31**, 37464–37471 (2023).
103. Gainutdinov RV, Volk TR, Zhang HH. Domain formation and polarization reversal under atomic force microscopy-tip voltages in ion-sliced $LiNbO_3$ films on SiO_2/$LiNbO_3$ substrates. *Appl Phys Lett* **107**, 162903 (2015).
104. Shao GH, Bai YH, Cui GX et al. Ferroelectric domain inversion and its stability in lithium niobate thin film on insulator with different thicknesses. *AIP Adv* **6**, 075011 (2016).
105. Volk T, Gainutdinov R, Zhang HH. Domain patterning in ion-sliced $LiNbO_3$ films by atomic force microscopy. *Crystals* **7**, 137 (2017).
106. Ma JN, Zheng NC, Chen PC et al. Tip-induced nanoscale domain engineering in x-cut lithium niobate on insulator. *Opt Express* **32**, 14801–14807 (2024).
107. Chezganov DS, Shur VY, Vlasov EO et al. Influence of the artificial surface dielectric layer on domain patterning by ion beam in MgO-doped lithium niobate single crystals. *Appl Phys Lett* **110**, 082903 (2017).
108. Chezganov DS, Vlasov EO, Neradovskiy MM et al. Periodic domain patterning by electron beam of proton exchanged waveguides in lithium niobate. *Appl Phys Lett* **108**, 192903 (2016).
109. Ito H, Takyu C, Inaba H. Fabrication of periodic domain grating in $LiNbO_3$ by electron beam writing for application of nonlinear optical processes. *Electron Lett* **27**, 1221–1222 (1991).
110. Nutt ACG, Gopalan V, Gupta MC. Domain inversion in $LiNbO_3$ using direct electron-beam writing. *Appl Phys Lett* **60**, 2828–2830 (1992).
111. Restoin C, Darraud-Taupiac C, Decossas JL et al. Ferroelectric domain inversion by electron beam on $LiNbO_3$ and Ti: $LiNbO_3$. *J Appl Phys* **88**, 6665–6668 (2000).
112. Restoin C, Darraud-Taupiac C, Decossas JL et al. Electron-beam poling on Ti: $LiNbO_3$. *Appl Opt* **40**, 6056–6061 (2001).
113. Shur VY, Chezganov DS, Smirnov MM et al. Domain switching by electron beam irradiation of Z^+-polar surface in Mg-doped lithium niobate. *Appl Phys Lett* **105**, 052908 (2014).
114. Chezganov DS, Smirnov MM, Kuznetsov DK et al. Electron beam domain patterning of MgO-doped lithium niobate crystals covered by resist layer. *Ferroelectrics* **476**, 117–126 (2015).
115. He J, Tang SH, Qin YQ et al. Two-dimensional structures of ferroelectric domain inversion in $LiNbO_3$ by direct electron beam lithography. *J Appl Phys* **93**, 9943–9946 (2003).
116. Volk TR, Kokhanchik LS, Gainutdinov RV et al. Domain formation on the nonpolar lithium niobate surfaces under electron-beam irradiation: a review. *J Adv Dielectr* **8**, 1830001 (2018).
117. Kurimura S, Shimoya I, Uesu Y. Domain inversion by an electron-beam-induced electric field in *MgO: LiNbO*$_3$, *LiNbO*$_3$ and *LiTaO*$_3$. *Jpn J Appl Phys* **35**, L31–L33 (1996).
118. Mizuuchi K, Yamamoto K. Domain inversion in $LiTaO_3$ using an ion beam. *Electron Lett* **29**, 2064–2066 (1993).
119. Chezganov DS, Vlasov EO, Gimadeeva LV et al. Growth of isolated domains induced by focused ion beam irradiation in congruent lithium niobate. *Ferroelectrics* **508**, 16–25 (2017).
120. Chezganov DS, Vlasov EO, Pashnina EA et al. Domain patterning of non-polar cut lithium niobate by focused ion beam. *Ferroelectrics* **559**, 66–76 (2020).
121. Li XJ, Terabe K, Hatano H et al. Nano-domain engineering in $LiNbO_3$ by focused ion beam. *Jpn J Appl Phy* **44**, L1550–L1552 (2005).
122. Nikolaeva EV, Shur VY, Dolbilov MA et al. Formation of nanoscale domain structures and abnormal switching kinetics in lithium niobate with surface layer modified by implantation of copper ions. *Ferroelectrics* **374**, 73–77 (2008).
123. Kokhanchik LS, Borodin MV, Shandarov SM et al. Periodic domain structures formed under electron-beam irradiation in $LiNbO_3$ plates and Ti: $LiNbO_3$ planar waveguides of the Y cut. *Phys Solid State* **52**, 1722–1730 (2010).
124. Krasnokutska I, Tambasco JLJ, Peruzzo A. Submicron domain engineering in periodically poled lithium niobate on insulator. (2021).
125. Ying CYJ, Muir AC, Valdivia CE et al. Light-mediated ferroelectric domain engineering and micro-structuring of lithium niobate crystals. *Laser Photonics Rev* **6**, 526–548 (2012).
126. Hou PP, Zhi YN, Liu LR. Laser-induced preferential domain nucleation in hafnium-doped congruent lithium niobate crystal. *Appl Phys A* **99**, 105–109 (2010).
127. Dierolf V, Sandmann C. Direct-write method for domain inversion patterns in $LiNbO_3$. *Appl Phys Lett* **84**, 3987–3989 (2004).

128. Wang WJ, Kong YF, Liu HD et al. Light-induced domain reversal in doped lithium niobate crystals. *J Appl Phys* **105**, 043105 (2009).
129. Wengler MC, Heinemeyer U, Soergel E et al. Ultraviolet light-assisted domain inversion in magnesium-doped lithium niobate crystals. *J Appl Phys* **98**, 064104 (2005).
130. Valdivia CE, Sones CL, Mailis S et al. Ultrashort-pulse optically-assisted domain engineering in lithium niobate. *Ferroelectrics* **340**, 75–82 (2006).
131. Sones CL, Wengler MC, Wengler MC et al. Light-induced order-of-magnitude decrease in the electric field for domain nucleation in MgO-doped lithium niobate crystals. *Appl Phys Lett* **86**, 212901 (2005).
132. Zhi YN, Liu DA, Qu WJ et al. Wavelength dependence of light-induced domain nucleation in MgO-doped congruent $LiNbO_3$ crystal. *Appl Phys Lett* **90**, 042904 (2007).
133. Sones CL, Muir AC, Ying YJ et al. Precision nanoscale domain engineering of lithium niobate via UV laser induced inhibition of poling. *Appl Phys Lett* **92**, 072905 (2008).
134. Steigerwald H, Ying YJ, Eason RW et al. Direct writing of ferroelectric domains on the *x*-and *y*-faces of lithium niobate using a continuous wave ultraviolet laser. *Appl Phys Lett* **98**, 062902 (2011).
135. Boes A, Steigerwald H, Yudistira D et al. Ultraviolet laser-induced poling inhibition produces bulk domains in MgO-doped lithium niobate crystals. *Appl Phys Lett* **105**, 092904 (2014).
136. Zisis G, Martinez-Jimenez G, Franz Y et al. Laser-induced ferroelectric domain engineering in $LiNbO_3$ crystals using an amorphous silicon overlayer. *J Opt* **19**, 084010 (2017).
137. Muir AC, Sones CL, Sones CL et al. Direct-writing of inverted domains in lithium niobate using a continuous wave ultra violet laser. *Opt Express* **16**, 2336–2350 (2008).
138. Boes A, Crasto T, Steigerwald H et al. Direct writing of ferroelectric domains on strontium barium niobate crystals using focused ultraviolet laser light. *Appl Phys Lett* **103**, 142904 (2013).
139. Boes A, Sivan V, Ren GH et al. Precise, reproducible nano-domain engineering in lithium niobate crystals. *Appl Phys Lett* **107**, 022901 (2015).
140. Jia YC, Wang SX, Chen F. Femtosecond laser direct writing of flexibly configured waveguide geometries in optical crystals: fabrication and application. *Opto-Electron Adv* **3**, 190042 (2020).
141. Xu XY, Wang TX, Chen PC et al. Femtosecond laser writing of lithium niobate ferroelectric nanodomains. *Nature* **609**, 496–501 (2022).
142. Shur VY, Kosobokov MS, Makaev AV et al. Dimensionality increase of ferroelectric domain shape by pulse laser irradiation. *Acta Mater* **219**, 117270 (2021).
143. Wang TX, Xu XY, Yang L et al. Fabrication of lithium niobate fork grating by laser-writing-induced selective chemical etching. *Nanophotonics* **11**, 829–834 (2022).
144. Li G. Periodically poled ridge waveguides and photonic wires in $LiNbO_3$ for efficient nonlinear interactions (University of Paderborn, Paderborn, 2010).
145. Lin JT, Yao N, Hao ZZ et al. Broadband quasi-phase-matched harmonic generation in an on-chip monocrystalline lithium niobate microdisk resonator. *Phys Rev Lett* **122**, 173903 (2019).
146. Chen MW, Wang CY, Tian XH et al. Wafer-scale periodic poling of thin-film lithium niobate. *Materials* **17**, 1720 (2024).
147. Luke K, Kharel P, Reimer C et al. Wafer-scale low-loss lithium niobate photonic integrated circuits. *Opt Express* **28**, 24452–24458 (2020).
148. Yan CL, Gu BS, Zhao S et al. Red and green light generation in TPPLNOI ridge optical waveguide with 1550 nm picosecond laser. *Opt Commun* **529**, 129023 (2023).
149. Ye XN, Liu SJ, Chen YP et al. Sum-frequency generation in lithium-niobate-on-insulator microdisk via modal phase matching. *Opt Lett* **45**, 523–526 (2020).
150. Henry A, Barral D, Zaquine I et al. Correlated twin-photon generation in a silicon nitride loaded thin film PPLN waveguide. *Opt Express* **31**, 7277–7289 (2023).
151. Chen JY, Sua YM, Fan H et al. Modal phase matched lithium niobate nanocircuits for integrated nonlinear photonics. *OSA Continuum* **1**, 229–242 (2018).
152. Lu CY, Zhang YT, Qiu J et al. Highly tunable birefringent phase-matched second-harmonic generation in an angle-cut lithium niobate-on-insulator ridge waveguide. *Opt Lett* **47**, 1081–1084 (2022).
153. Wang L, Li LQ, Zhang XT et al. Type I phase matching in thin film of lithium niobate on insulator. *Results Phys* **16**, 103011 (2020).
154. Okubo S, Onae A, Nakamura K et al. Offset-free optical frequency comb self-referencing with an f-2f interferometer. *Optica* **5**, 188–192 (2018).
155. Sun Y, Tu HH, Boppart SA. Nonlinear optical imaging by detection with optical parametric amplification (invited paper). *J Innov Opt Health Sci* **16**, 2245001 (2023).
156. Denzer W, Hancock G, Hutchinson A et al. Mid-infrared generation and spectroscopy with a PPLN ridge waveguide. *Appl Phys B* **86**, 437–441 (2007).
157. Baxter GW, He Y, Orr BJ. A pulsed optical parametric oscillator, based on periodically poled lithium niobate (PPLN), for high-resolution spectroscopy. *Appl Phys B* **67**, 753–756 (1998).
158. César-Cuello J, Carnoto I, García-Muñoz LE et al. Towards a lithium niobate photonic integrated circuit for quantum sensing applications. *Photonics* **11**, 239 (2024).
159. Manzoni C, Cerullo G. Design criteria for ultrafast optical parametric amplifiers. *J Opt* **18**, 103501 (2016).
160. Shimizu S, Kobayashi T, Kazama T et al. PPLN-based optical parametric amplification for wideband WDM transmission. *J Light Technol* **40**, 3374–3384 (2022).
161. Zhao J, Ma CX, Rüsing M et al. High quality entangled photon pair generation in periodically poled thin-film lithium niobate waveguides. *Phys Rev Lett* **124**, 163603 (2020).
162. Boyd RW. *Nonlinear Optics* (Academic Press, San Diego, 2003).
163. Hickstein DD, Carlson DR, Kowligy A et al. High-harmonic generation in periodically poled waveguides. *Optica* **4**, 1538–1544 (2017).
164. Wu TH, Ledezma L, Fredrick C et al. Visible-to-ultraviolet frequency comb generation in lithium niobate nanophotonic waveguides. *Nat Photonics* **18**, 218–223 (2024).
165. Rao DSS, Jensen M, Grüner-Nielsen L et al. Shot-noise limited, supercontinuum-based optical coherence tomography. *Light Sci Appl* **10**, 133 (2021).
166. Canalias C, Pasiskevicius V. Mirrorless optical parametric oscillator. *Nat Photonics* **1**, 459–462 (2007).
167. Boes A, Chang L, Nguyen T et al. Enhanced nonlinearity in

lithium niobate on insulator (LNOI) waveguides through engineering of lateral leakage. In *CLEO: QELS_Fundamental Science 2019*, FW3B. 4 (Optica Publishing Group, 2019); http://doi.org/10.1364/CLEO_QELS.2019.FW3B.4.

168. Wu Y, Wei JJ, Zeng C et al. Efficient sum-frequency generation of a yellow laser in a thin-film lithium niobate waveguide. *Opt Lett* **49**, 2833–2836 (2024).
169. Umeki T, Tadanaga O, Asobe M. Highly efficient wavelength converter using direct-bonded PPZnLN ridge waveguide. *IEEE J Quantum Electron* **46**, 1206–1213 (2010).
170. Parameswaran KR, Kurz JR, Roussev RV et al. Observation of 99% pump depletion in single-pass second-harmonic generation in a periodically poled lithium niobate waveguide. *Opt Lett* **27**, 43–45 (2002).
171. Cho CY, Lai JY, Hsu CS et al. Power scaling of continuous-wave second harmonic generation in a MgO: PPLN ridge waveguide and the application to a compact wavelength conversion module. *Opt Lett* **46**, 2852–2855 (2021).
172. Berry SA, Carpenter LG, Gray AC et al. Zn-indiffused diced ridge waveguides in MgO: PPLN generating 1 watt 780 nm SHG at 70% efficiency. *OSA Continuum* **2**, 3456–3464 (2019).
173. Choge DK, Chen HX, Guo L et al. Simultaneous second-harmonic, sum-frequency generation and stimulated Raman scattering in MgO: PPLN. *Materials* **11**, 2266 (2018).
174. Choge DK, Chen HX, Guo L et al. Double-pass high-efficiency sum-frequency generation of a broadband orange laser in a single MgO: PPLN crystal. *Opt Mater Express* **9**, 837–844 (2019).
175. Kumar SC, Sukeert, Ebrahim-Zadeh M. High-power continuous-wave mid-infrared difference-frequency generation in the presence of thermal effects. *J Opt Soc Am B* **38**, B14–B20 (2021).
176. Mazzotti D, De Natale P, Giusfredi G et al. Difference-frequency generation in PPLN at 4.25 μm: an analysis of sensitivity limits for DFG spectrometers. *Appl Phys B* **70**, 747–750 (2000).
177. Hirano M, Morimoto A. Optical frequency comb generation using a quasi-velocity-matched Fabry-Perot phase modulator. *Opt Rev* **15**, 224–229 (2008).
178. Kim DS, Arisawa M, Morimoto A et al. Femtosecond optical pulse generation using quasi-velocity-matched electrooptic phase modulator. *IEEE J Sel Top Quantum Electron* **2**, 493–499 (1996).
179. Wang Y, Shi JH, Yang JL et al. Design of quasi-velocity-matched $LiTaO_3$ phase modulator. *Proc SPIE* **4220**, 135–138 (2000).
180. Guo FZ, Yu CT, Chen L et al. Quasi-velocity-matched electrooptic phase modulator for the synthesis of ultrashort optical pulses. *IEEE J Quantum Electron* **33**, 879–882 (1997).
181. Chen XF, Shi JH, Chen YP et al. Electro-optic Solc-type wavelength filter in periodically poled lithium niobate. *Opt Lett* **28**, 2115–2117 (2003).
182. Lu YQ, Zhu YY, Ming NB. Electro-optic effect and its applications in periodically poled optical superlattice $LiNbO_3$. In *Technical Digest. Summaries of Papers Presented at the Conference on Lasers and Electro-Optics. Postconference Edition. CLEO '99. Conference on Lasers and Electro-Optics* (*IEEE Cat. No. 99CH37013*) 448 (IEEE, 1999); http://doi.org/10.1109/CLEO.1999.834429.
183. Ding TT, Zheng YL, Chen XF. On-chip solc-type polarization control and wavelength filtering utilizing periodically poled lithium niobate on insulator ridge waveguide. *J Lightw Technol* **37**, 1296–1300 (2019).
184. Sohler W, Hu H, Ricken R et al. Integrated optical devices in lithium niobate. *Opt Photonics News* **19**, 24–31 (2008).
185. Morgan D, Paige EGS. *Surface Acoustic Wave Filters: with Applications to Electronic Communications and Signal Processing* (Academic Press, Amsterdam, 2007).
186. Gronewold TMA. Surface acoustic wave sensors in the bioanalytical field: recent trends and challenges. *Anal Chim Acta* **603**, 119–128 (2007).
187. Länge K, Rapp BE, Rapp M. Surface acoustic wave biosensors: a review. *Anal Bioanal Chem* **391**, 1509–1519 (2008).
188. Lee SW, Rhim JW, Park SW et al. A micro rate gyroscope based on the SAW gyroscopic effect. *J Micromech Microeng* **17**, 2272–2279 (2007).
189. Pekarčíková M, Hofmann M, Menzel S et al. Investigation of high power effects on Ti/Al and Ta-Si-N/Cu/Ta-Si-N electrodes for SAW devices. *IEEE Trans Ultrason Ferroelectr Freq Control* **52**, 911–917 (2005).
190. Lu YQ, Zhu YY, Chen YF et al. Optical properties of an ionic-type phononic crystal. *Science* **284**, 1822–1824 (1999).
191. Friend J, Yeo LY. Microscale acoustofluidics: microfluidics driven via acoustics and ultrasonics. *Rev Mod Phys* **83**, 647–704 (2011).
192. Boes A, Yudistira D, Rezk A et al. Ultraviolet direct domain writing on 128° YX-cut $LiNbO_3$: for SAW applications. In *Proceedings of 2013 Joint IEEE International Symposium on Applications of Ferroelectric and Workshop on Piezoresponse Force Microscopy* 272–274 (IEEE, 2013); http://doi.org/10.1109/ISAF.2013.6748659.
193. Chen X, Ali Mohammad M, Conway J et al. High performance lithium niobate surface acoustic wave transducers in the 4–12 GHz super high frequency range. *J Vac Sci Technol B* **33**, 06F401 (2015).
194. Yudistira D, Benchabane S, Janner D et al. Surface acoustic wave generation in *Z X*-cut $LiNbO_3$ superlattices using coplanar electrodes. *Appl Phys Lett* **95**, 052901 (2009).
195. Gustafsson MV, Aref T, Kockum AF et al. Propagating phonons coupled to an artificial atom. *Science* **346**, 207–211 (2014).
196. O'Connell AD, Hofheinz M, Ansmann M et al. Quantum ground state and single-phonon control of a mechanical resonator. *Nature* **464**, 697–703 (2010).
197. Olsson III RH, El-Kady I. Microfabricated phononic crystal devices and applications. *Meas Sci Technol* **20**, 012002 (2009).
198. Huang CP, Zhu YY. Piezoelectric-induced polariton coupling in a superlattice. *Phys Rev Lett* **94**, 117401 (2005).
199. Yudistira D, Boes A, Dumas B et al. Phonon-polariton entrapment in homogenous surface phonon cavities. *Ann Phys* **528**, 365–372 (2016).
200. Barry IE, Ross GW, Smith PGR et al. Microstructuring of lithium niobate using differential etch-rate between inverted and non-inverted ferroelectric domains. *Mater Lett* **37**, 246–254 (1998).
201. Yudistira D, Boes A, Graczykowski B et al. Nanoscale pillar hypersonic surface phononic crystals. *Phys Rev B* **94**, 094304 (2016).
202. Ying CYJ, Sones CL, Peacock AC et al. Ultra-smooth lithium niobate photonic micro-structures by surface tension reshaping.

Opt Express **18**, 11508–11513 (2010).

Acknowledgements

This research was supported by the Australian Research Council Centre of Excellence in Optical Microcombs for Breakthrough Science COMBS (CE230100006), and the Australian Research Council grants DP220100488 and DE230100964, funded by the Australian Government. The authors would like to thank Dr. Reinhard Geiss and Mr. Andres Saenz Perez for providing the polarization contrast image (PCM) in Fig.8c, which was taken in the lab facility of Abbe Center of Photonics at Friedrich Schiller University, Jena, Germany.

Author contributions

All authors commented on the manuscript.

The review article was conceptualized by Andreas Boes (A.B.) and Arnan Mitchell (A.M.). Jackson J. Chakkoria (J.J.C.) and Aditya Dubey (A.D.) conducted the literature review and compiled the initial draft. All authors contributed to drafting, revising, and editing the manuscript. A.B. and J.J.C. coordinated the project.

Competing interests

The authors declare no competing financial interests.

Scan for Article PDF